Western redcedar on the Olympic Peninsula: Locating this culturally, economically, and

ecologically important species using remote sensing methodologies

Ally Kruper

A thesis

submitted in partial fulfillment of the

requirements for the degree of

Master of Science

University of Washington

2024

Committee:

Bernard T. Bormann

Robert J. McGaughey

Marc L. Miller

Program Authorized to Offer Degree:

Environmental and Forest Sciences

University of Washington

Abstract

Western redcedar on the Olympic Peninsula: Locating this culturally, economically, and
ecologically important species using remote sensing methodologies

Ally Kruper

Chair of the Supervisory Committee:

Bernard T. Bormann

School of Environmental and Forest Sciences

Western redcedar (*Thuja plicata* Donn ex D. Don) is a culturally, economically, and ecologically
important species native to the Pacific Northwest. Abundance of western redcedar on the
landscape today is a fraction of what it was historically due to a combination of overharvesting in
the 20th century, incompatibility with short-rotation forestry, cedar browse by ungulates, and a
documented western redcedar dieback phenomenon linked to climate change. Restoring cedar
will rely on our ability to map western redcedar trees on the landscape, particularly using tools
such as remote sensing that have larger spatial coverage capabilities. This study used metrics
derived from UAV (unmanned aerial vehicle) multispectral imagery and LiDAR to train a model
to identify and map western redcedar trees on the west side of the Olympic Peninsula, with a
focus on the T3 Watershed Experiment in the Olympic Experimental State Forest. Models were

trained based on different combinations of data collection years, study areas, multispectral

imagery and LiDAR, and the portion of the crown represented by LiDAR point clouds clipped

for each tree (small cylinder vs. only the top 3 m). Generally, models achieved the highest

accuracies when subset by study area and when only the top 3 m of the LiDAR trees were used.

The best and most robust model achieved an accuracy of 86%. In addition to species

classification, indices derived from the multispectral imagery were used as proxies to assess

cedar health. However, no clear conclusions could be drawn due to confounding factors related

to study area differences, the data limitations of using spectral signatures for this type of work,

and the complexities inherent in tree health; all of which were discussed in depth for use in

future research. Overall, this study demonstrated that UAV LiDAR and multispectral imagery

are powerful tools in mapping western redcedar trees over relatively large areas, including robust

methodology on how to achieve this work on an individual tree basis.

Table of Contents

List of Tables and Figures

1. Introduction

1.1. Western Redcedar: Species Background and Distribution

Western redcedar (*Thuja plicata* Donn ex D. Don) is a cherished coniferous tree native to the Pacific Northwest with high cultural significance, timber value, and importance for wildlife. Western redcedar is a member of the cypress family (*Cupressaceae*), is a long-lived species, and is the largest diameter native tree in the Pacific Northwest (R. Van Pelt, 2007). It is considered a generalist compared to other species; it can grow both directly after a disturbance and in mature forests, has high stress tolerance, can survive nutrient poor soils, and is both sun and shade tolerant (Antos et al., 2016). It tends to grow as a part of mixed-species stands, rather than monocultures (Antos et al., 2016). Although western redcedar exhibits high tolerances to abiotic and biotic disturbances, it has a slower growth rate compared to neighboring species, and longer rotations to grow its higher timber value heartwood to merchantable size (Antos et al., 2016). The population of western redcedar on the landscape today is estimated to be a fraction of what it was historically (R. Van Pelt, 2007).

1.2. Cultural, Economical, and Ecological Importance of Western Redcedar

Western redcedar has immense cultural, economic, and ecological importance. It has great tribal significance throughout its range, leading it to be deemed a top "culture keystone species" (Garibaldi & Turner, 2004). Erna Gunther, renowned ethnobotanist, stated in her book "Ethnobotany of Washington" that "Throughout the whole Northwest the wood most extensively used by the Indians is cedar…Equally as useful as the wood is the bark of the cedar tree, in fact there is no single item so ubiquitous in the Indian household" (Gunther, 1973, p. 20). Western redcedar can be used to make a variety of items, including canoes, boxes, house posts and

planks, clothing, plates, mats, ropes, baskets, and more (Gunther, 1973; Johnson et al., 2021;

Turner & Bell, 1971). In addition to material goods, cedar is also used in medicine, for

ceremonies, and has great spiritual significance; for example, the Skagit burned cedar at night to

scare away the ghost after death (Gunther, 1973). A 2018 study focused on land management

philosophies of First Nation individuals compared to ecologically-based foresters found that,

while ecologically-based foresters had a spiritual connection to nature broadly, First Nations

individuals had a "unique spiritual relationship with western redcedar that is linked to both

everyday and ceremonial practices" (Zahn et al., 2018). In 1993, members of the Skokomish

Tribe detailed the tribe's concern over the then current state of western redcedar in an article

titled, "Too Long, Too Silent: The Threat to Cedar and the Sacred Ways of the Skokomish"

(Pavel et al., 1993).

Many indigenous communities have actively managed their land for timber for canoes,

bark, or totem poles (Johnson et al., 2021), to promote the growth of particularly understory

species such as camas, huckleberry, and beargrass through the use of fire (Shebitz et al., 2009; N.

J. Turner & Turner, 2007), or for other cultural resources using traditional ecological knowledge.

This is a practice that continues. Tribes typically view protecting the forest not as leaving the

forest as no-touch reserves, but rather the active involvement of people in managing the forest

(Gordon et al., 2013).

In addition to tribal importance, western redcedar has general economic importance.

Western redcedar is known as an especially durable and attractive wood, granting it economical

as well as cultural significance. Western redcedar is known for its natural decay resistance,

which has been linked with specific lignans (Morris & Stirling, 2012). Its wood is used in

roofing as shakes and shingles, with additional uses in products such as poles, posts, and paper

pulp (Nesom, 2001). During the peak of the timber industry in Forks, WA, in the 1970s, a person could make \$25,000 to \$30,000 a year cutting cedar bolts—cubes of cedar wood from stumps and downed logs oftentimes used in shakes and shingle making (J. Van Pelt, 2007). In Canada, western redcedar is considered to be "one of the most valuable commercial tree species in British Columbia," with the industry generating over \$1 billion (CAD) in economic activity annually as of 2018 (Gregory et al., 2018). In North America, it is estimated that western redcedar sells for two to four times the amount of other commercial conifers (Antos et al., 2016). It has a consistently higher pond value (estimated value when delivered to the timber mill) compared to other native species (Jones, n.d.) (Figure 1).
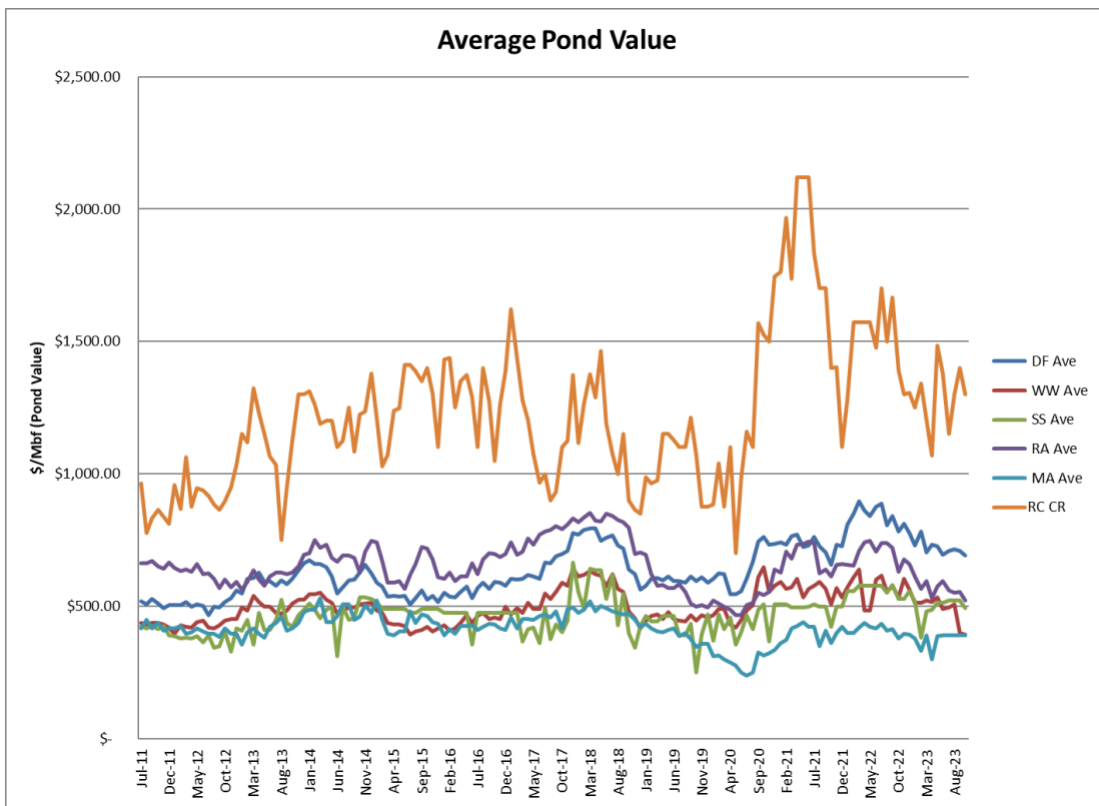
Figure 1. Average pond values (value at timber mill) for different timber species over time from July 2011 to August 2023. Prices are in U.S. dollars per 1,000 board feet. Different line colors represent different species: orange is western redcedar (RC CR), blue is Douglas-fir (DF), red is western hemlock (WW), green is Sitka spruce (SS), purple is red alder (RA), and turquoise is bigleaf maple (MA). Data and graph provided by Keith Jones from the WA DNR Product Sales and Leasing Division.

One investigation surrounding the economics of processing western redcedar shakes and shingles in local mills, as requested by the Clallam County Economic Development Council, stated that, "For more than 150 years, the manufacture of shingle and shake roofing materials from western red cedar has been an important industry in western Washington" (Mason et al., 2005). Furthermore, western redcedar is in many ways an ideal species for small-woodland owners to plant for timber and/or other ecological value. It does well on land with known laminated wood rot (western redcedar is resistant), if they are worried about insects/diseases, and/or if they are looking for a species with low management intensity required (Kline et al., 2017).

Finally, in addition to both cultural and economic importance, western redcedar has great ecological importance. Northern spotted owl (*Strix occidentalis caurina*) nests can be found in western redcedar trees, particularly in forests that exhibit old growth characteristics (Hershey et al., 1998). Compared to western hemlock (*Tsuga heterophylla* (Raf.) Sarg.), the soil under western redcedar trees have been found to have greater soil pH, exchangeable calcium, and heavier organic horizons (Alban, 1969). And, because western redcedar is generally more long-lived compared to other native species, it can provide complex structures of increased value compared to shorter lived species (Franklin & Spies, 1983).

Furthermore, public agencies have an interest in western redcedar. The USDA Forest Service Supervisor for the Olympic National Forest expressed interest in a tool that would allow for successful mapping of western redcedar on the landscape. The Olympic National Forest has a significantly higher percentage of land designated as late-successional reserve compared to other national forests, as well as a high potential for carbon storage (Bioregional Assessment of Northwest Forests, 2020). Successful mapping of western redcedar could positively impact the management of late-successional habitat and aid in maximizing carbon storage, especially

because it is well suited for longer rotations when peak volume increment occurs. As another public agency, the Washington State Department of Natural Resources (WA DNR) includes among its priorities "Keeping our forests healthy and productive through management, regulation, and partnerships" (DNR Strategic Plan 2022-2025, 2022). Mapping a key species, western redcedar, could aide in managing for healthy, resilient forests. It would additionally provide information regarding the extent, size, and health of cedar for timber purposes.

1.3. Western Redcedar Decline

Given the cultural, economic, and ecological importance of western redcedar, investigating the biogeography of cedar and sustaining cedar populations across the landscape is imperative, because the abundance of western redcedar today has declined compared to its historical level. This decline is due to overharvesting in the 20th century, a lack of replanting by forest managers due to the increased risk of ungulate browsing, incompatibility with the standard 30–40-year Douglas-fir rotations, and a documented dieback linked to the ongoing consequences of climate change, such as warmer and drier conditions.

In 1966, across the Olympic Peninsula counties Clallam, Jefferson, and Grays Harbor, there was an estimated 6 billion harvestable board feet of western redcedar; by 1977, this number decreased to 3.4 billion board feet due to timber harvesting and cedar's slow regrowth (Bolsinger, 1979). Western redcedar is more susceptible to ungulate browsing than other native conifers, leading to general uncertainty in planting cedar (Cornwell, 2022; Stroh et al., 2008). In addition to these primary factors, other factors such as illegal timber theft (Trick, 2012), also play a role.

There is a documented western redcedar dieback that is likely linked to drought, rising temperatures, and declining snowpack; furthermore, a recent study directly linked the dieback to warmer and drier summers (Andrus et al., 2023; Fischer, 2019). While it has not been directly linked to climate change, these are all conditions exacerbated by climate change. As symptoms of this dieback, redcedar trees have notably recently been experiencing negative health-related effects such as thinning crowns and dead tops (Fischer, 2019). These ongoing effects are concerning, particularly given the lack of knowledge surrounding the exact extent of the cedars affected. Currently, a group from the Puyallup Extension of Washington State University are tracking this phenomenon through a Western Redcedar Dieback Map added to by citizen scientists ("Western Redcedar Dieback," n.d.). It is not only important to map and track individual western redcedar trees on the landscape, but to be able to accurately assess and map evidence of plant stress as well. The above factors in combination suggest, without intervention, the increasing decline of western redcedar on the landscape and the need for further studies on western redcedar.

1.4. Remote Sensing for Forest Inventory Measurements

Remote sensing can aid in a solution. Forest inventory measurements (species identification, tree height, basal area, etc.) are essential to forestry. Yet, ground measurements can be time-consuming and costly, especially at large spatial coverages. Thus, many resource scientists today use remotely sensed data, connecting remote sensing to ground measurements to ultimately increase forest inventory measurements on a broader spatial coverage. These studies take many forms. For instance, one study performed in Alaska used remotely sensed data to classify and map forest types located spatially between existing USDA Forest Service, Forest

Inventory and Analysis plots (Shoot et al., 2021); and another study used it to estimate aboveground biomass in boreal forests across North America (Margolis et al., 2015). In particular, remotely sensed data has been used to classify tree species in a variety of different experiments, usually on small-scale studies that typically lack a clear application (Fassnacht et al., 2016).

LiDAR (light detection and ranging) is a type of remotely sensed data that involves shooting laser pulses towards the ground. Energy from those laser pulses then reflects back to the sensor producing a range and intensity value, allowing for the creation of what are called point clouds, a 3D representation of the objects that reflected the laser pulses (Michałowska & Rapiński, 2021).

Use of LiDAR in forest management has increased in recent years due to its high accuracy and resolution, as well its potential broad applications (Hudak et al., 2009). LiDAR has been used by a multitude of studies to perform species classification specifically (Korpela et al., 2010; Kruper et al., 2022; Liang et al., 2007). Similar to LiDAR, multispectral imagery has also been extensively used to perform species classification (Heikkinen et al., 2010; Zhang & Hu, 2012). Multispectral imagery captures wavelengths within the electromagnetic spectrum that include the classic color bands of red, green, and blue, but with additional 'colors' defined that are useful for discrimination of tree species and health. The newly defined colors often extend into the near infrared. The combination of these two types of remotely sensed data—LiDAR and multispectral imagery—has been used by several studies for species classification (Dalponte et al., 2012; Holmgren et al., 2008; Hologa et al., 2021).

The use of drones, or UAVs (unmanned aerial vehicles), to collect remote sensing data such as LiDAR and multispectral imagery has also greatly increased in recent years due to the

advances in drone technology and the potential for high-density, high-resolution data that can be produced. UAV LiDAR is normally higher resolution than airborne or satellite LiDAR simply because the drone flies closer to the target trees. Recent research has been carried out using drone LiDAR to perform different forest inventory measurements, including DBH (diameter at breast height) and tree height measurements, individual tree delineation, and species classification (da Cunha Neto et al., 2021; Feng et al., 2022; Gong et al., 2023; Yin & Wang, 2019). Higher resolution UAV LiDAR and multispectral imagery was used in this research to perform species classification with the ultimate goal of mapping western redcedar trees.

1.5. Use of Multispectral Imagery as a Proxy for Cedar Health

Although the primary goal of this research was to perform species classification, a secondary goal was to include a relative health assessment using the multispectral imagery as a proxy to aid in understanding the decline in western redcedar health. UAV multispectral imagery has been utilized in other contexts to monitor plant health and stress at fine spatial scales, particularly in the context of agricultural crops (Backoulou et al., 2011; Sosa-Herrera et al., 2019; Vlachopoulos et al., 2022). However, it has been used in the context of assessing tree stress as well (Dash et al., 2018; Fraser & Congalton, 2021).

Plants that have more chlorophyll production have different spectral signatures than plants with less chlorophyll production. There are existing multispectral imagery indices that can highlight these differences, which have been used in past studies to assess relative plant health/stress with the assumption that increased chlorophyll equates to increased production. It should be noted that these use the multispectral imagery as indirect measurements of plant health, typically relative to another point in time and as an indication of overall plant growth and

yield. In this study, the multispectral imagery was used as an assessment tool for crown stress in western redcedar trees at a precise moment of time and should not be viewed as a direct assessment of individual tree health.

1.6. The T3 Watershed Experiment

The Type 3 (T3) Watershed Experiment played a large role in this research. This study is a 20,000-acre operational-scale experiment in the Olympic Experimental State Forest, on the western side of the Olympic Peninsula. This study is working to expand the management toolbox by testing novel forest management approaches in both upland and riparian areas and comparing them to standard practice for state lands management (Bobsin et al., 2023). A key component of this study was to engage researchers, managers, stakeholders, and tribes from the very beginning to create prescriptions that were economically and operationally feasible, scientifically valid and interesting, and important and informed by the communities that use this forestland for their personal, cultural, or economic wellbeing. This study is a collaboration led by the Washington State Department of Natural Resources (DNR) and the University of Washington (UW) through the Olympic Natural Resources Center.

1.7. Tribal Engagement, Learning-Based Collaboration, and the T3 Learning Groups

A key goal of the T3 Watershed Experiment was to engage stakeholders and tribes from the beginning to ensure their input, values, knowledge, and needs were incorporated directly into the study plan. In order to do this, the T3 team completed semi-structured interviews, three two-hour focus groups, several field tours, two conferences, and countless informal discussions. This led to better relationships and rapport with these participating groups. This engagement was done

through learning-based collaboration (LBC) "where natural resource managers and practitioners, researchers, stakeholders, and tribes engage with one another focusing on asking and answering questions about options and effects of management choices through scientifically valid comparisons" (Minkova et al., 2024). LBC is needed to achieve ecosystem wellbeing, which consists of both environmental and community wellbeing, and is ultimately necessary for increasing adaptive capacity (Bobsin et al., 2023).

Through the process of LBC, the T3 team was able to engage with several coastal tribes who have ceded, non-ceded, traditional hunting and gathering grounds, or Usual and Accustomed lands in the T3 watersheds. This included working closely with the Quileute Tribe, initially through the Tribal Council through a government-to-government process and eventually working directly with the Quileute Tribe's Natural Resources Department. A key concern was the lack of accessible and mature cedar on the landscape. This directly influenced the T3 experimental study design. It also led us to directly work with the Quileute Natural Resources Department on this study, aiming to identify the location of cedar trees across the landscape and ultimately assist the Tribe for cedar bark harvesting.

The T3 Experiment additionally uses LBC by aiding in the facilitation of the T3 Learning Groups. These self-assembled groups, of which there are eight total ranging from invasive species to carbon sequestration, include people from diverse backgrounds who focus on a particular topic of interest in which they want to collaborate, discuss, and pursue in relation to the T3 Watershed Experiment (Minkova et al., 2024). These group meetings allow for the exchange of ideas and group learning between different people with different backgrounds and goals. This study regularly worked with and received feedback from the Cedar Learning Group.

1.8. Overall Study Aims

This research study had the following primary aims:

1. Create Random Forest-based models using information derived from UAV LiDAR and/or multispectral imagery to distinguish between western redcedar and other tree species, focusing on the T3 Watershed Experiment.

2. Use the multispectral imagery signatures as proxies to investigate cedar health.

The first aim of creating Random Forest-based models had additional sub aims to further tease out optimal model specifications. This study used ground and remote sensing data from two different study areas: areas within the OESF (Olympic Experimental State Forest) and more limited areas of the Olympic National Forest (ONF). UAV LiDAR and multispectral imagery were acquired for denser cedar plots within the OESF and all the plots within the ONF. However, no multispectral imagery data were acquired on about half of the OESF plots, in the less cedar dense plots. The limitations on the remote sensing data and study area differences led to the creation of ten different models, and the sub aims of comparing study area differences, comparing LiDAR and multispectral imagery models vs. LiDAR alone, and comparing models using LiDAR metrics from the top 3 m of trees vs. a full small cylinder clip of the tree.

The overall purposes of this model making include a pre-treatment assessment of western redcedar in the T3 Experiment, improving methodology to connect ground plots to remote sensing data and create clean training datasets on an individual tree level, creating maps for the Quileute Tribe Natural Resources Department, and for potential future research in understanding the biogeography of western redcedar.

2. Methods

2.1. Study Areas

The study areas for this experiment included: 1) the Olympic Experimental State Forest (OESF) near the Hoh and Clearwater watersheds outside of Forks, WA, with a high concentration of ground plots within the sub-boundaries of the T3 Watershed Experiment (T3); and 2) the Olympic National Forest (ONF) near Humptulips, WA (Figure 2). The majority of the ground plots were within the T3 experimental watershed (31/50; 62%), followed by the ONF (13/50; 26%), and finally the OESF directly outside of the T3 experimental watersheds (6/50; 12%). The goal in establishing plots in the ONF was to expand the range of western redcedar tree sizes obtained. In addition to size, these large trees are much older, with many expected to be over 200 years old on the ONF study area, while they were between approximately 40- to 70-years-old on the OESF study areas.
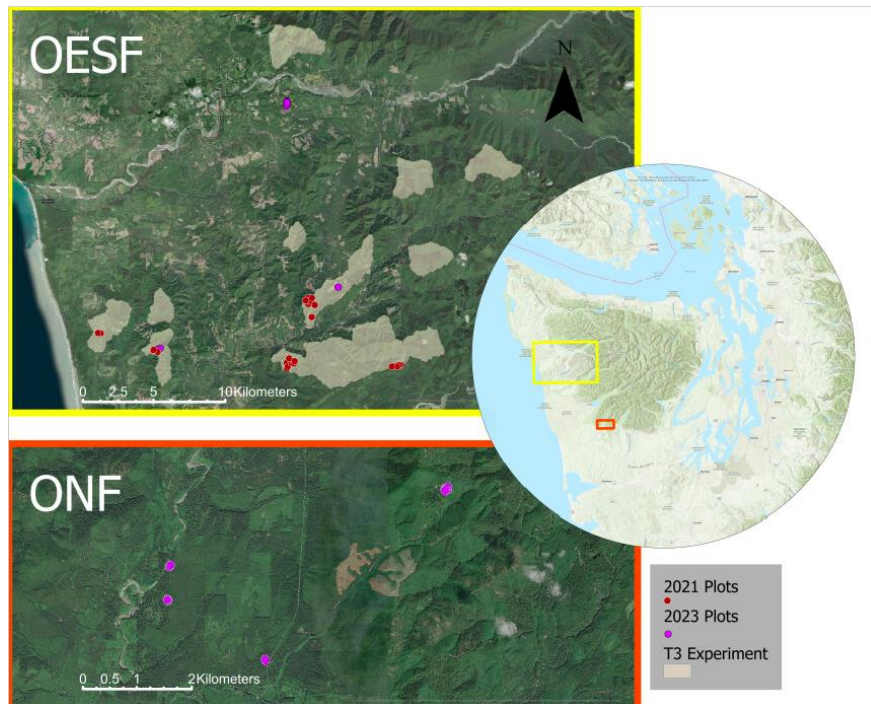
Figure 2. Map of the two primary study areas: the OESF (Olympic Experimental State Forest; top left) and the ONF (Olympic National Forest; bottom left) on the Olympic Peninsula, WA, USA. Locations of these study areas are marked via the boxes on the regional map: the OESF area in yellow and the ONF area in orange. Plots established in 2021 are indicated by the red circles and plots established in 2023 are indicated by the pink circles. The watersheds of the T3 study are indicated by the semi-transparent polygons within the OESF area map.

2.1.1. The Olympic Experimental State Forest and T3 Watershed Experiment

The Olympic Experimental State Forest and the T3 Watershed Experiment are state trust lands managed by the Washington Department of Natural Resources. About 80% of these forests have been harvested once and many stands are 40- to 70-years-old and have a very dense, closed canopy structure (Figure 3). Forest composition is typically dominated by western hemlock and planted Douglas-fir (*Pseudotsuga menziesii* Mirb. Franco), with other species occurring periodically: silver fir (*Abies amabilis* (Dougl. ex Loud.) Dougl.), Sitka spruce (*Picea sitchensis* Bong. Carriere), red alder (*Alnus rubra* Bong.), and western redcedar. Mid- to lower-canopy species typically consists of vine maple (*Acer circinatum* Pursh.) and cascara buckthorn (F*rangula purshiana* (DC.) A. Gray).

As the T3 Experiment is located within the OESF, data from those areas will hereafter be referred to as simply "OESF" as a general term.

Figure 3. Photograph of the OESF area. Photo credit Evan Gray.

2.1.2. The Olympic National Forest

The Olympic National Forest land is managed by the USDA Forest Service in accordance with the Olympic National Forest 1990 Land and Resource Management Plan as amended by the

1996 Northwest Forest Plan, which designated all Olympic National Forest land as one of the following: Late Successional Reserve, Adaptive Management Area, or Riparian Reserve (*Olympic National Forest - Planning*, n.d.). This study area was located outside of Humptulips, WA. These forests are much older than the OESF stands and typically have a relatively open canopy (Figure 4). Overstory species composition consists primarily of western hemlock and western redcedar, with the occasional silver fir, Sitka spruce, or red alder. Lower-canopy species typically consisted of vine maple.

Figure 4. Photograph of the ONF area.

2.2. Ground Data

The ground data for this study consisted of two primary datasets: one from 2021 and the other from 2023. These two sets of ground data differed in primary location, typical tree species measured, stand age, and plot size; however, the field protocol was otherwise the same for both. The 2021 ground data was collected in the T3 Experiment for the purpose of representing the pre-treatment conditions. It consisted of 27 circular ground plots of radius 17.68 m. The most common tree species in those plots were western hemlock and Douglas-fir with only a scattering

of cedar (Figure 5; a). Given the cedar focus of this study, the 2023 circular plots were established in locations that had particularly high abundance of western redcedar trees. Thus, these plots primarily consisted of western redcedar and western hemlock trees (Figure 5; b and c). These plots were also variable in size and were 5-20 m in radius depending on the number of western redcedar trees in the area.
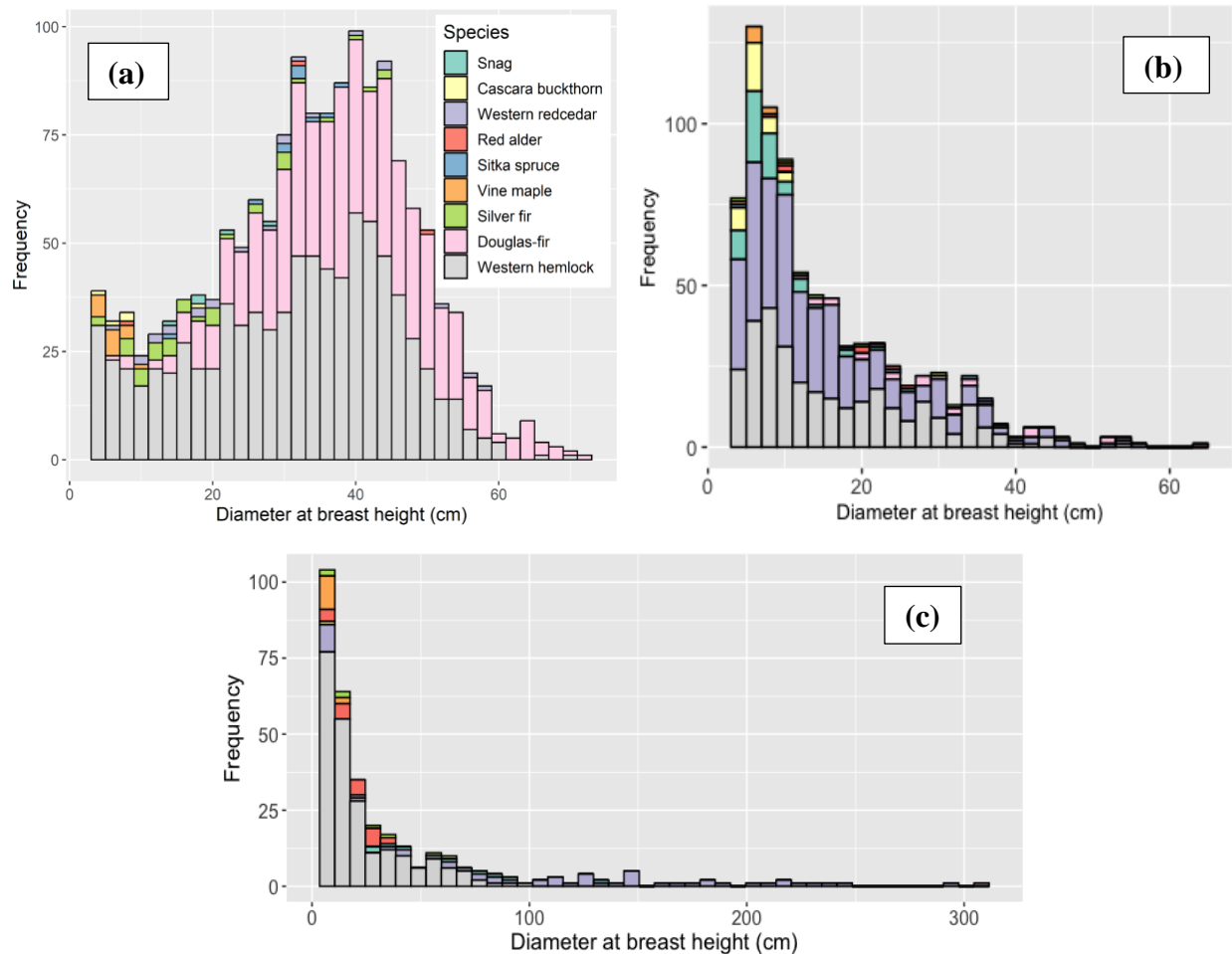
Figure 5. Frequency of trees species measured in ground plots binned based on their DBH (diameter at breast height; cm). Trees are separated to show study area and year differences: the top left graph **(a)** depicts data from 2021 collected in the OESF (McGaughey et. al, 2024), the top right data from the 2023 OESF cedar plot data **(b)**, and the bottom middle the 2023 ONF data **(c)**. Trees are colored based on tree species (snags are light green; cascara buckthorn light yellow; western redcedar purple; red alder red; Sitka spruce blue; vine maple orange; silver fir light green; Douglas-fir pink; and western hemlock light grey).

For both years, the following data were collected for every tree in the plot: tree species, diameter (cm) measured at breast height (1.37 m; DBH), yes/no if LiDAR visible (subjectively based on technician's assessment; "Yes" defined as a tree that is visible from above and has a crown that is not majorly overlapping with another tree), distance and azimuth from the tree to a given point (a reference tree for the 2021 data; the center point of the plot for the 2023 data), and an anomaly number. For the 2021 ground data, distance and azimuth was measured using a logger's tape and a compass; for the 2023 ground data, a Haglöf Vertex Laser Geo (Långsele, Sweden) and corresponding transponder allowed for the use of ultrasound in distance measurements. The distance and azimuth from each tree to a reference point allowed for the creation of stem maps, or the relative spatial position of each tree in each plot.

Anomaly numbers consisted of the following: (0) No anomaly; (1) Dead tree; (2) Leaning tree; (3) Tree shares base with another tree/forked tree; (4) Tree is on a stump; (5) Tree is less than 0.5 m away from another tree; (6) Tree displays signs of bear damage; (7) Tree has a broken top; (8) Anomaly was not assessed; and (9) DBH estimated. The anomaly number 9 (DBH estimated) was particularly common for the large cedar trees in the ONF. DBH was measured on the uphill side of the tree, and for these larger cedar trees the DBHs and slopes were sufficiently large that it was impossible to measure the DBH the traditional way due to height and arm span limitations of the field technicians; instead, one half (or one quarter in extreme circumstances) of the tree was measured and then multiplied to estimate the final DBH number. Ground data was filtered to remove trees with anomaly code 1 (dead tree) and any that were not marked as LiDAR visible in the field for the purposes of matching field trees (i.e. trees from the ground data) to LiDAR segmented trees.

Location estimates were taken for every plot using a Javad Triumph 2, a survey-grade GNSS receiver (San Jose, CA, USA). At every location, the Javad Triumph 2 continually collected data for at least twenty minutes. A study done in 2017 in the Pacific Northwest that used a similar receiver, Javad Triumph-1, and ran it for twenty minutes under dense canopy conditions had a mean horizontal accuracy of 1.76 m (McGaughey et al., 2017). The Javad Triumph 2 data from this study appeared to have similar accuracies although it was occasionally larger than that, which was expected due to the impact of overhead vegetation in the denser canopy conditions.

Additionally, for the 2023 cedar plots, data was collected on cedar health. For every western redcedar tree in a plot, the health of the tree was assessed using the following code system: (1) Healthy; (2) Yellowing Canopy; (3): Browning Canopy; (4) Top dieback; and (5) Heat damage (scorched tips of needles). These health codes were adapted from those used for the Washington State University Puyallup Western Redcedar Dieback Map project in order to maintain consistency with already-existing standards ("Western Redcedar Dieback," n.d.). However, it was determined in the field that these health assessments were not sufficiently accurate to use in modeling. Oftentimes, the trees were too dense and the canopy base height too high to make an accurate assessment from the ground. Thus, these health codes were not used in the analyses.

2.3. LiDAR and Multispectral Imagery Data

All LiDAR and multispectral imagery data, from both the years 2021 and 2023, were collected and initially processed by West Fork Environmental, a natural resources consulting firm out of Tumwater, WA. The data was flown using a DJI Matrice 600 Pro Hexacopter

(Shenzhen, China). The 2021 LiDAR data was measured using a Quanergy M8 sensor (San Jose, CA, USA) that emits up to 1.3 million points per second with up to three returns per pulse. The aggregate pulse density for this 2021 data was 556 pulses m^{-2} with a standard deviation of 519 pulses m^{-2}. The hexacopter with the Quanergy M8 sensor was flown at a height above ground ranging 50-80 m depending on topography and vegetation. Total coverage of this 2021 data was approximately 167 ha in segments across the T3 Watershed Experiment.

The 2023 LiDAR data was collected using a Surveyor 32 LiDAR System by LiDAR USA (Alabama, USA) that emits up to 1.3 million points per second with up to two returns per pulse. The aggregate pulse density for this 2023 data was 1098 pulses m^{-2} with a standard deviation of 133 pulses m^{-2}. The hexacopter with the Quanergy M8 sensor was flown at a height above ground ranging 60 to 70 m depending on topography and vegetation. Total coverage of this 2023 data was approximately 24 ha in segments across the OESF and 14 ha in the ONF Humptulips area. The 2023 multispectral imagery data was collected using a AgEagle Altum-PT, which can capture up to two images per second. Multispectral bands captured include blue, green, red, red-edge, and near-infrared. The camera was flown on the hexacopter at 120 m above ground. Total coverage of the multispectral imagery data is approximately equal to the 2023 LiDAR coverage.

All LiDAR data was cleaned and prepped by the contractor: noise points were deleted, and ground points were classified.

2.4.1. Matching Ground to Remote Sensing Data: Total Plot Adjustment Based on LiDAR Data

The following matching, processing, and health analysis methods sections (2.4-3.0) are all in relation to the 2023 field, LiDAR, and multispectral imagery data. The 2021 data was

processed separately for an earlier publication (McGaughey et al., 2024) and underwent a separate, but similar, process, with a few notable exceptions which will be discussed as needed in the following sections.

The first step in modeling was matching the ground data to the remote sensing data. This was required to be able to train a Random Forest model that could successfully group (and predict) LiDAR—and, for some models, multispectral imagery—segmented trees as either western redcedar or not western redcedar. Given its higher GNSS accuracy over the Javad and multispectral imagery sensor, the LiDAR data were used as the locational standard. Additionally, the 3D LiDAR locations were superior to the 2D multispectral imagery. The matching of the ground trees to LiDAR segmented trees was completed in two parts: first, a larger overall plot adjustment, and then a finer individual tree adjustment.

To complete this overall plot level matching, LiDAR canopy height models (CHMs) were first created using the UAV LiDAR data. CHMs are the result of subtracting a digital terrain model from a digital surface model; they are essentially like laying a blanket over the forest canopy, and they allow for an easy 2D representation of the forest canopy, and thus, the individual tree locations. These CHMs were created using the 'lidR' (Roussel et al., 2020, 2024) and 'raster' (Hijmans, 2023) packages within R Studio version 4.3.0 (RStudio Team, 2023). The LiDAR point clouds were first normalized using a triangular irregular network (TIN) algorithm, and then converted to CHMs with a 0.5 m resolution and a TIN algorithm. Stem maps of individual trees in each plot, created using the ground data, were then matched to the CHMs on a plot-by-plot basis in ArcGIS Pro (Figure 6).
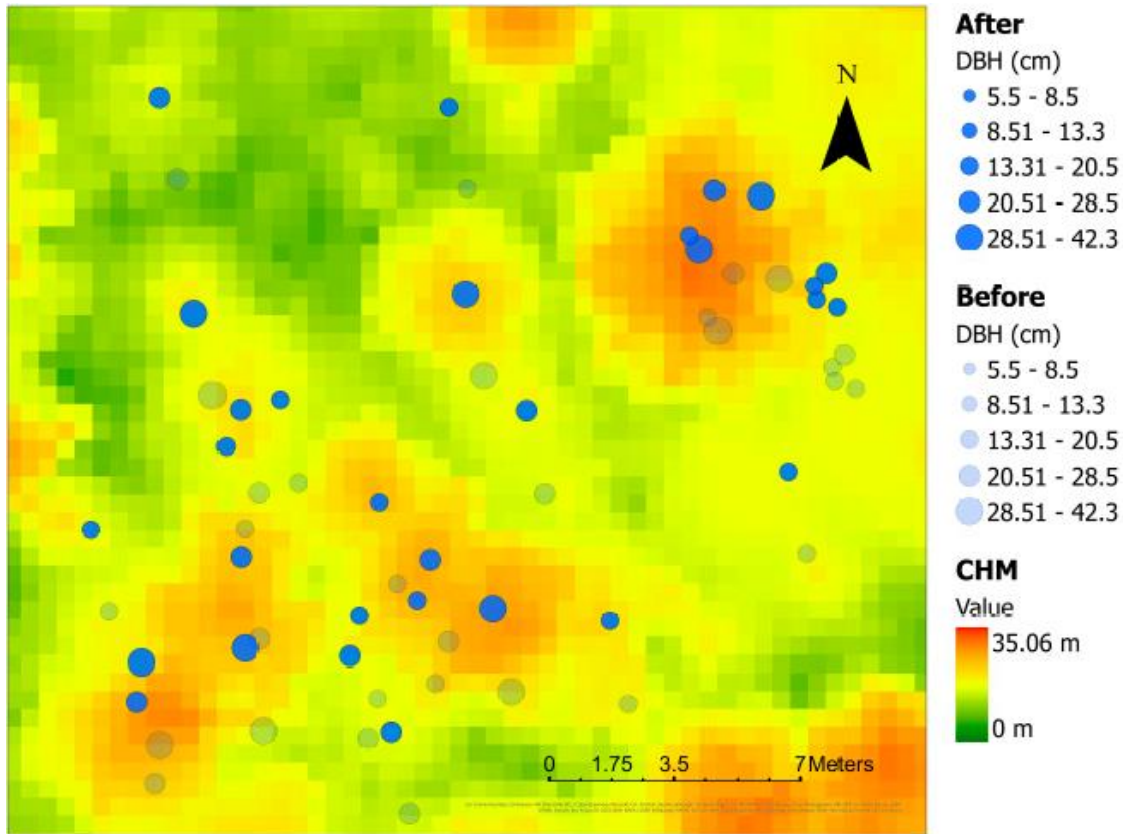
Figure 6. Example ground plot matched to a canopy height model (CHM). The CHM is colored by height, with the taller objects appearing more red and the shorter objects appearing more green. Individual trees measured in the plot are represented by the blue circles. The semi-transparent blue circles represent the location of trees before the plot level adjustment; the solid blue circles represent the location of trees after the plot level adjustment. Sizes of the blue circles are based on tree DBH. For visualization purposes, trees that were labeled as not LiDAR visible in the field and trees less than 15 cm DBH were filtered out and are not included in this figure.

2.4.2. Matching Ground to Remote Sensing Data: Individual Tree Adjustment Based on LiDAR

Data

Before the ground trees were matched to individual LiDAR trees, the ground trees were

prepped by using each tree's DBH to estimate tree height. This was completed using diameter-

height equations from the Forest Vegetation Simulator Pacific Northwest Coast (PN) Variant,

Olympic NF location (Donnelly et al., 2022). Canopy base height (CBH), min diameter, and max

diameter were all additionally estimated by multiplying height by the following ratios, in

corresponding order: 0.6, 0.16, and 0.16. The goal for these simple estimates was to produce "reasonable" tree models to help match the field and LiDAR trees.

Following the above plot level matching, individual field trees were matched to individual LiDAR trees in the program FUSION version 4.51 using its new plot and individual tree movement capabilities; Appendix H of the FUSION manual (McGaughey, 2023b). This was completed to help ensure clean training data. Every LiDAR tree was matched top and bottom (Figure 7). This top and bottom matching was completed due to the impact of leaning trees— many of the plots occurred on relatively steep terrain, leading to trees growing naturally with a lean. If this lean was not accounted for in data processing, it could lead to some trees being inaccurately clipped. Note that many trees did not have sufficient LiDAR pulse penetration through the canopy to connect to tree stems; in those situations, the stem of the tree was followed as far down to the ground as possible and then dropped to ground elevation directly below that point.
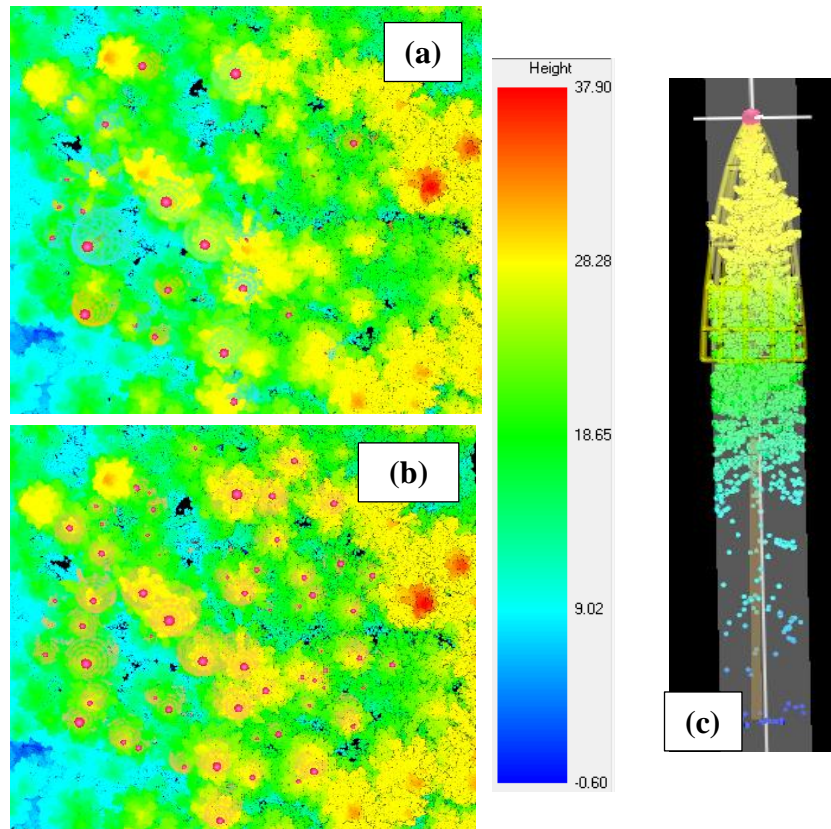
Figure 7. Example plot and tree from the individual tree level matching process. Top left **(a)** is a plot before individual trees ground trees were matched to LiDAR trees and bottom left **(b)** is the same plot after the matching process. Ground trees are represented by a cylindrical cone (size and shape based on estimated canopy base height and diameter) with a cylinder representing a stem coming out the bottom (length based on height of tree) and a red ball on top of the tree (size based on DBH). Middle right **(c)** is an example individual ground tree matched top and bottom to the LiDAR. Individual LiDAR points are colored by height in meters.

As ground trees were matched to LiDAR trees, the following status codes were added for each individual tree: (0) Ideal (everything good); (1) Not used (indicated in field notes as not LiDAR visible and/or dead); (2) Blended (tree appears to be under another tree's canopy/blended with another canopy to the extent that the tree top is indistinguishable); (3) Dead top; and (4) Incorrect (tree species highly likely incorrect). Status code 3 (dead top) was added because some of the ONF western redcedar trees had dead tops noticeable in the LiDAR that were missed in the field, likely due to poor visibility of the treetops from the ground (Figure 8).
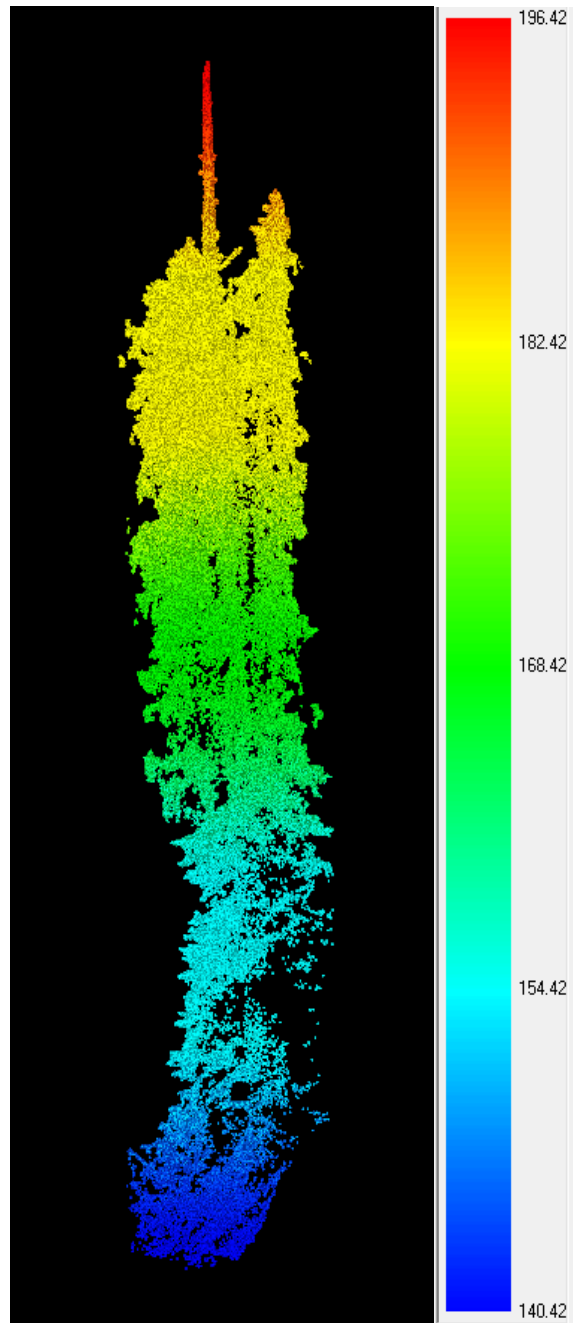
Figure 8. Example western redcedar with a notable dead top (status code 3) from the ONF study area. Colored by elevation in meters.

Status code 4 (species highly likely incorrect) was used sparingly but did occur periodically

(Figure 9). All trees with status code other than 0 or 3 were filtered out of the dataset and were

not used in further processing.
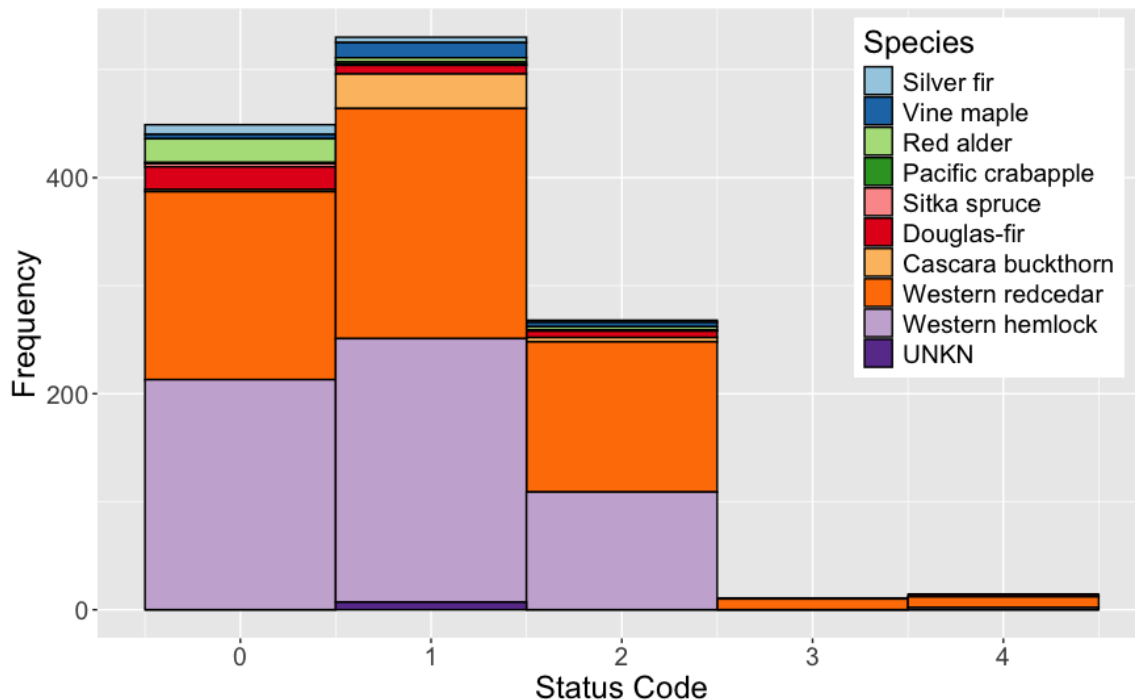
Figure 9. Histogram of the status codes of individual trees. Status codes represent the following: (0) Everything good; (1) Not moved (indicated in field not LiDAR visible and/or dead); (2) Tree appears to be under another tree's canopy/blended with another canopy to the extent that the tree top is indistinguishable; (3) Dead top; (4) Tree species highly likely incorrect. Tree species are represented by the following colors: light blue for silver fir, dark blue for vine maple, light green for red alder, dark green for Pacific crabapple, pink for Sitka spruce, red for Douglas-fir, light orange for cascara buckthorn, dark orange for western redcedar, light purple for western hemlock, dark purple for unknown species (UNKN).

2.5. Matching Ground to Remote Sensing Data: Matching Field Trees to Multispectral Imagery

As discussed above, the ground trees were moved and matched to the LiDAR, as opposed to the multispectral imagery, for the higher accuracy LiDAR locational data and the ease of matching 3D imagery compared to 2D imagery. Because of this, little work needed to be completed in terms of lining up the ground trees with the multispectral imagery. The locational data of the ground trees from the LiDAR matching process were used for all the trees, and each image tile of the multispectral imagery was moved to match the LiDAR CHMs. This process was

completed in ArcGIS Pro on an individual image tile basis, and typically involved little movement. The greatest movement required was approximately 4 m, with most tiles only requiring 0 to 3 m of movement. This appeared sufficient for ground matched trees to line up with the canopies visible in the multispectral imagery.

2.6. Remote Sensing Data Processing: LiDAR

Processing of the full extent of the UAV LiDAR data was completed in R Studio using the 'Fusionwrapr' package (McGaughey, n.d.) and adapted already-existing code (McGaughey, 2023a). This processing involved automatically segmenting all trees within the UAV drone LiDAR extent and then running cloud metrics on each individual tree (See Appendix A for metrics descriptions). These LiDAR segmented trees were then put aside to be used later when predicting species outside of the known plot trees.

Next, cloud metrics were run on the matched ground to LiDAR trees. This process used already-existing code (McGaughey, 2024b) that was adapted for this particular analysis. Notable, significant changes to that code include the following. First, the ONF cedar trees were so large (in terms of LiDAR point returns for each tree) that the processing was taking too long and warranted another method. A smaller diameter, initial cylindrical tree clip was the final solution (Figure 10; a). This worked well on the larger trees but appeared too narrow for the smaller trees; thus, it was decided that trees under 15 cm DBH would be clipped based on their crown diameter divided by two, whereas the trees above 15 cm DBH would be clipped based on their crown diameter divided by four. Clipping the trees conservatively like this helped increase confidence that the LiDAR points isolated by the tree clipping did indeed belong to the tree in question, as opposed to neighboring tree(s).

However, upon randomly selecting and examining the final results of the above clipping, it was determined that the initial cylindrical clips were still insufficient in terms of isolating only the tree in question (Figure 10; b). This is due to the structure of the OESF forests. In particular, the cedar trees within the OESF tended to be slightly shorter than the surrounding Douglas-fir and western hemlock trees, which was problematic in ensuring that the LiDAR trees were clipped to only include a single tree each—ideally no branches from neighboring trees. Thus, a new conical clipping was added and completed following the above initial cylindrical clipping (Figure 10; c).

This conical clipping appeared successful in isolating the cedar trees without overlapping branches from neighboring trees. However, initial attempts resulted in the western hemlocks being clipped too liberally at their tops, resulting in part of their iconic 'droopy top' being cut off. Additionally, the conical clipping appeared more successful if varied by tree size. Thus, the final angle of the conical clip was variable based on tree species and tree size (diameter), with western hemlocks and larger trees receiving a larger angle clip. These angle numbers were decided qualitatively by visually accessing the results for each species at the extremes of the different tree sizes. There is admittedly more optimization that could be done here, as there is a trade-off between cutting off points for some trees and getting too many points for other trees.
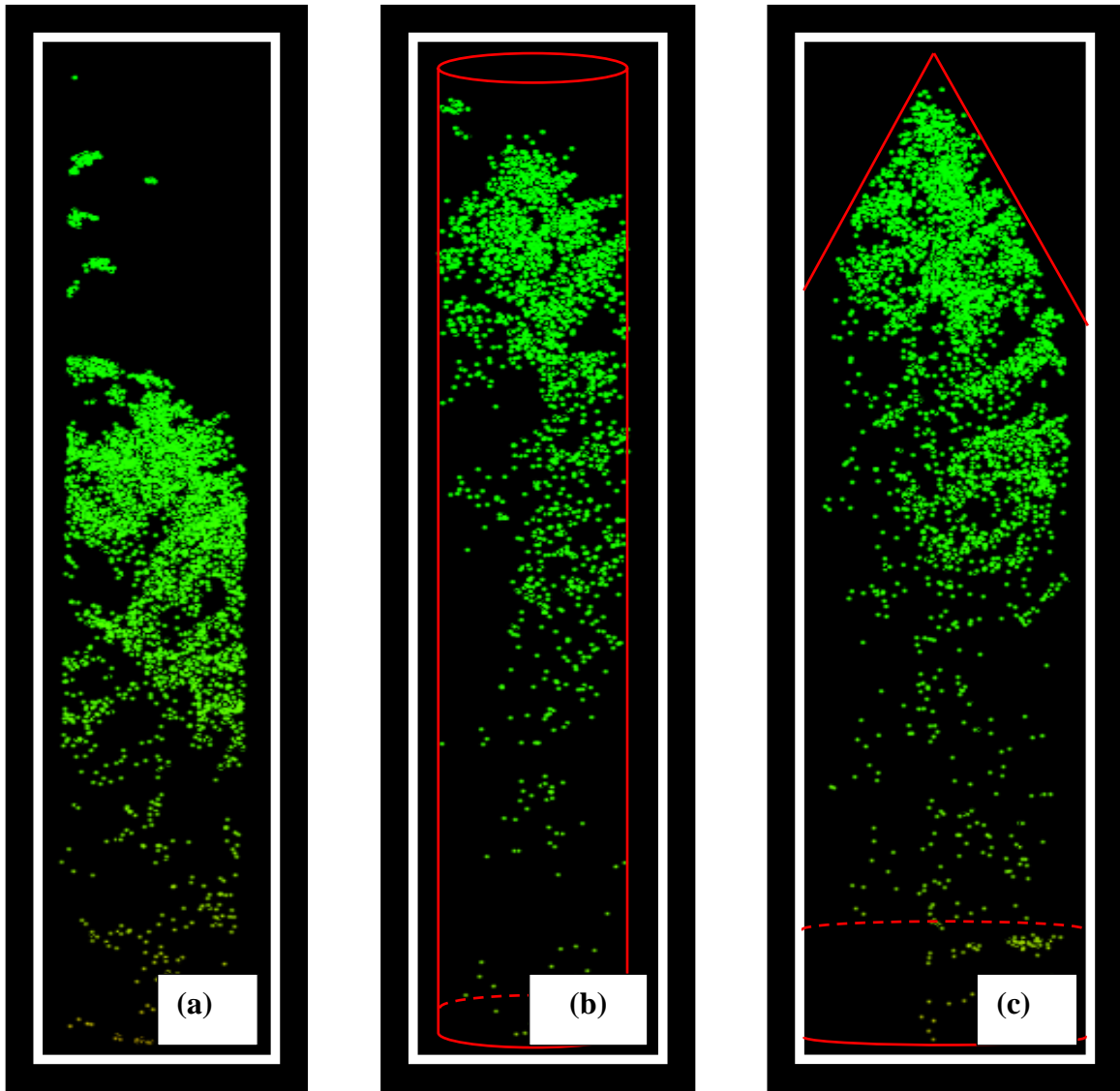
Figure 10. Example of clipping process with point clouds of an individual western redcedar tree: **(a)** depicts the cedar tree before the clippings, **(b)** the cedar tree after the first smaller cylinder clip with red lines representing the cylindrical clip boundaries, and **(c)** the cedar tree after the subsequent conical clipping with red lines representing the conical clip boundaries.

This above clipping process (Figure 10), both the variable initial cylindrical clipping and the subsequent conical clipping, were additionally run on the 2021 matched LiDAR to ground trees. As mentioned earlier, these trees were initially processed before this study for a different study and thus went through a slightly different matching process than the 2023 trees. However,

27

for consistency, the 2021 matched LiDAR trees were processed using the same clipping process as the 2023 trees above.

After locations were pinned down and the clipping process completed, cloud metrics were computed for each individual tree. Two different datasets of cloud metrics were created: one for the full tree resulting in this process, and the other for the top 3 m only of each tree (Figure 11). The top 3 m was chosen as an option as that was found to be more useful in previous analyses (McGaughey et al., 2024), although with western redcedar's unique shape when viewed as a full profile it was unclear which would perform superior in later model making. Thus, the two datasets were created to test this.
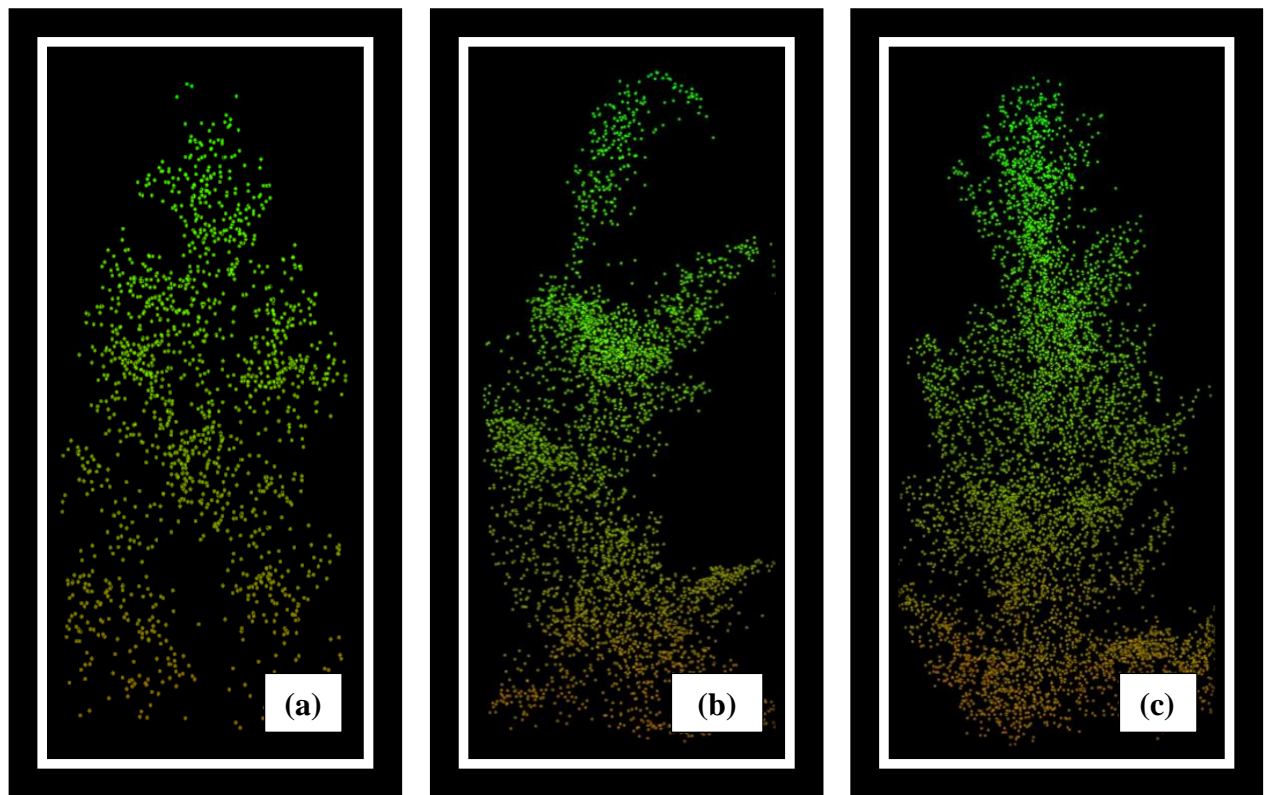
Figure 11. Example ground matched LiDAR trees, clipped to only the top 3 m, of the following species from left to right: western redcedar **(a)**, western hemlock **(b)**, and Douglas-fir **(c)**.

Much of the process discussed in this section, with the notable exception of the utilized cone clipping logic, was used and discussed in further detail in McGaughey et. al, 2024.

2.7. Remote Sensing Data Processing: Multispectral Imagery

Initial processing included first stretching the delivered multispectral imagery bands to produce 16-bit values, and then combining those bands to produce different relevant indices. This process was completed using adapted already-existing code (McGaughey, 2024a). The original multispectral bands delivered for the study include a red band (668 nm center, 14 nm bandwidth), green band (560 nm center, 27 nm bandwidth), blue band (475 nm center, 32 nm bandwidth), near-infrared (NIR) band (842 nm center, 57 nm bandwidth), red-edge band (717 nm center, 12 nm bandwidth), panchromatic band, and a long-wave infrared (LWIR) band (*AgEagle Altum-PT Brochure*, 2022). The panchromatic and LWIR bands were not used for the purpose of this study. Indices that were created from the initial bands were adopted from a study that examined new and existing indices for the purpose of estimating leaf area index (Xie et al., 2018). They were chosen for the purpose of this study due to their correlation to plant health/productivity variables such as chlorophyll content and overall vegetation health. A full list of these indices and associated meanings can be found in Appendix B. Average values from these indices were used as the multispectral metrics for this study.

These metrics were extracted from the multispectral imagery for each individual ground matched tree. This process was completed using the 'terra' package (Hijmans, 2024) within R Studio. Like with the LiDAR matched trees, only the trees with status code 0 (no issues in FUSION individual tree matching) and 3 (dead top) were used in the multispectral imagery extraction to ensure clean training data. For each tree, the mean value of each multispectral index

was extracted for that tree based on a 2D circular area estimate of the tree's crown (Figure 12). The diameter for the circular estimate was calculated as the tree's minimum crown diameter divided by two. The minimum crown diameter was calculated for each field tree based on that tree's height (calculated based on FVS equations) multiplied by the ratio of 0.16. Dividing that result (the minimum crown diameter) by two for the purpose of multispectral imagery metric extraction was determined through qualitatively looking at the resulting crowns vs. the crowns visible in the multispectral imagery and wanting to be on the conservative side, only extracting metrics for the exact tree in question.

Additionally, while checking the metrics extraction areas, a shadow effect was observed (Figure 12). This appeared particularly evident for the younger, shorter trees that were overshadowed by their neighbors. To avoid this shadow effect biasing the model, trees under 20 cm DBH in the OESF area and under 30 cm DBH in the ONF area were filtered out of the dataset. These DBH sizes were determined through the random selection of trees of various sizes and the corresponding observed shadow effect.
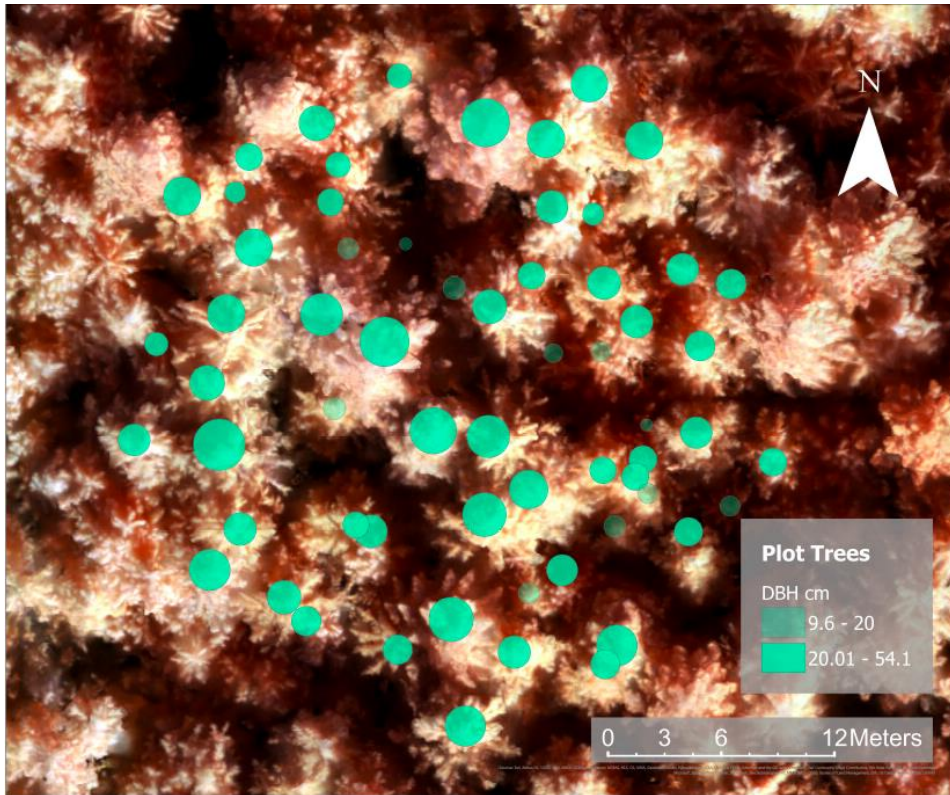
Figure 12. Individual ground trees represented by green circles overlaid on an example multispectral image. The circles are equal to the size of the extraction circle used to extract multispectral imagery metrics associated with each ground tree. To highlight the shadow effect observed in smaller trees, trees under 20 cm are semi-transparent, and trees above that threshold are more solid-colored. This multispectral image is from one of the OESF plots and is a NIR/red-edge/green image with NIR in the 'red' (band 1) position, red-edge in the 'green' (band 2) position, and green in the 'blue' (band 3) position.

For trees outside of ground plots, the locations of individual trees were determined using the tree locations from the automatically segmented LiDAR dataset. This locational information was used because it was already processed and would lead to easier combining of the multispectral and LiDAR data in later model making. For the multispectral imagery metrics extraction, the circular extraction sizes were determined using equations that used individual tree heights, as tree diameter and species information were not available for those trees. To determine the ideal circle extraction size, the following process was performed: first, DBH vs. tree height

data from the LiDAR matched trees dataset was graphed to determine an ideal cutoff of when the

DBH/height relationship became exponential as opposed to linear, and the height at that point

was recorded at approximately 45 m. This cutoff was important because the relationship between

height and DBH—directly related to crown size—changes as a tree grows older; older trees, such

as the trees in the ONF area, may continue to grow wider but not taller at the same rate as the

younger trees. Thus, those trees require a different equation to calculate their ideal extraction

circle. All trees below the 45 m cutoff height had their height divided by the simple number 30

and trees above 45 m were divided by 50. The results of these division were used as the diameter

for the multispectral imagery metrics extraction circle. The numbers 30 and 50 were determined

through a visual examination of the results.

2.8. Species Classification Model Making

      Final species classification modeling using the extracted LiDAR and multispectral

imagery metrics was conducted using a Random Forest algorithm and the R Studio packages

'tidymodels' (Kuhn & Wickham, 2020) and 'ranger' (Wright & Ziegler, 2017). Source code was

adapted from another analysis (Silge, 2020). Models were two class classifications and divided

the trees as either 'Western redcedar' or 'Other'. The 'Other' category primarily consisted of

Douglas-fir and western hemlock for the OESF area, and primarily just western hemlock for the

ONF area (Figure 5). Because of the relatively low sample size of western redcedar trees

compared to other species, the 'Other' category was downsampled to match the number of

western redcedar trees (Figure 13).
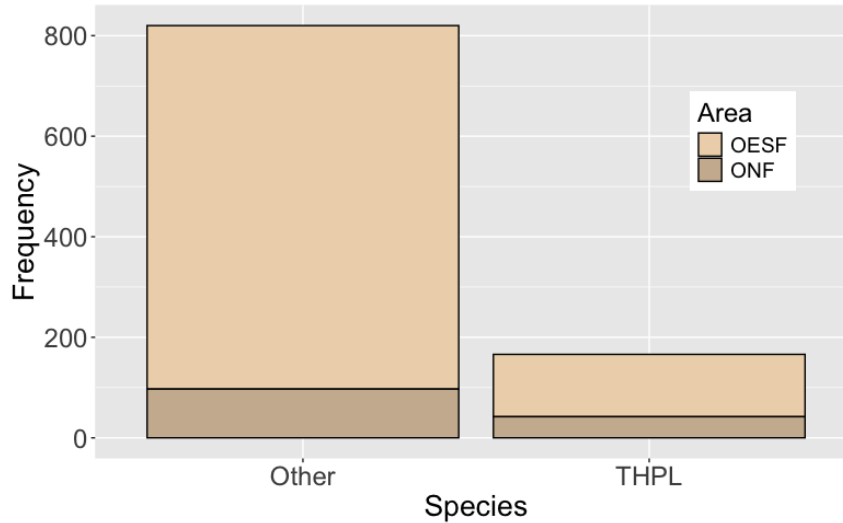
Figure 13. Histogram depicting the data imbalance between the number of western redcedar ("THPL") trees vs. "Other" tree species. The bins are colored by study area, with trees from the OESF area presented as a lighter brown than those from the ONF area. This histogram was created using only data from the LiDAR only model.

This sample size imbalance was particularly important as Random Forest is known to be susceptible to data imbalances. Out of the many LiDAR intensity-related metrics, only mean intensity was used in the final model making. This is because of the differences in intensity values between the years 2021 and 2023 due to the different LiDAR sensors used, and is discussed further in Appendix C.

The data was split into training and testing data using a 75/25 split. Other splits were tested and had relatively little effect on the model results, with the 75/25 having an about average and more conservative result compared to the other splits tested: 76% for a 75/25 split, 77% for an 80/20 split, and 79% for a 70/30 split for one model tested. Thus, the default 75/25 split was kept. After splitting into training and testing datasets, 10-fold cross-validation was performed for the purpose of tuning the model hyperparameters: the training data was split into ten equal parts; nine of those parts were used in tuning to determine the optimal numbers for the

hyperparameters 'mtry' (the number of predictors used in each decision tree split) and 'min_n' (the minimum number of samples needed to perform another split), and the final one was set aside to assess the results of the tuning. This 10-fold cross-validation helped ensure the Random Forest algorithm was not overfitted on the training data, which could lead to overinflated accuracy results. The number of decision trees for the Random Forest algorithm was set to 1,000.

For each model, variable importance was used to determine the top predictors in the model. The top ten important variables were pulled and tested for correlation in descending order of variable importance. This was completed until there were five uncorrelated predictors for the model. If less than five predictors were uncorrelated out of the top ten, the correlated predictors were removed, and the model was re-run with only the uncorrelated variables. This process was repeated until the top five predictors were identified. Metrics resulting from each model include model accuracy and ROC-AUC (receiver operating characteristics-area under the curve). ROC-AUC is an alternative model assessment that some find superior to overall accuracy (Huang & Ling, 2005). ROC-AUC results are not discussed in-depth for the purpose of this study but are included for those who may be interested.

Due to the various data limitations (ex: multispectral imagery coverage for 2023 data but not 2021 data) and the question of whether a full cylinder LiDAR clip vs. the top 3 m only performs better, in total ten models were completed (Table 1).

Table 1. List of all ten models

	Model
LiDAR only	Both areas, small cylinder
	Both areas, top 3 m
	OESF area only, small cylinder
	OESF area only, top 3 m
LiDAR and multispectral imagery	Both areas, top 3 m
	Both areas, small cylinder
	ONF area only, top 3 m
	ONF area only, small cylinder
	OESF area only, top 3 m
	OESF area only, small cylinder

2.9. Cedar Health Analysis Using Multispectral Imagery as Proxy

Originally, a cedar health analysis using cedar health codes from the field data and connecting those to multispectral imagery metrics to predict health indicators over a larger area was planned. However, this analysis was dropped because of an inability in the field to assign health codes, due to poor canopy visibility from the ground. Instead, exploratory analysis on the multispectral imagery metrics (from the field matched trees) using simple boxplots was conducted and revealed large spectral signature differences between the study areas OESF and ONF. This was then further explored through a multivariate analysis. This multivariate analysis was conducted in R Studio using statistical functions primarily from the 'vegan' package (Oksanen et al., 2022) and some adapted code (Bakker, 2024).

The multispectral imagery metrics were first relativized by range due to the different scales of the data and some of the indices having values less than one. An Euclidean distance measure was then applied to the response variables. Finally, a PCA (principal component analysis) was conducted on the data to compare western redcedar and western hemlock multispectral metrics across the two study areas. All other species were dropped due to low

sample sizes (Figure 5). The two primary axes were explored in relation to their likely driving explanatory variable: study area and species. Follow-up ANOVA (analysis of variance) tests were then conducted to test for correlation between these likely explanatory variable drivers and their corresponding related PCA axes.

3. Results

3.1. Species Classification of Western Redcedar

This analysis created strong predictor models. Due to the different combinations of data availability (ground plots and associated LiDAR for years 2021 and 2023 but only multispectral imagery coverage for the 2023 plots, two different study areas, and clipping to either a small cylinder or top 3 m) ten models were completed with the goal of determining optimal model data (Table 1). All models were relatively accurate with a range of 73-92% depending on the model (Table 2). In general, models with data from both study areas combined performed worse (accuracies of 78%, 79%, 76%, and 73%) than when the models were first subset by area: OESF (accuracies 82%, 86%, 80%, and 78%) and ONF (accuracies 92% and 92%). These study area differences match a pattern observed with the multispectral imagery metrics, albeit on a smaller scale. This pattern is discussed further in the Discussion section.

Table 2. List of models and corresponding accuracies (%) and ROC-AUC (receiver operating characteristics-area under the curve) scores

Model		Accuracy (%)	ROC-AUC score
LiDAR only	Both areas, small cylinder	78	86
	Both areas, top 3 m	79	83
	OESF area only, small cylinder	82	94
	OESF area only, top 3 m	86	94
LiDAR and multispectral imagery	Both areas, top 3 m	76	81
	Both areas, small cylinder	73	84
	ONF area only, top 3 m*	92	96
	ONF area only, small cylinder*	92	94
	OESF area only, top 3 m*	80	83
	OESF area only, small cylinder*	78	85

Adding multispectral imagery metrics to the LiDAR models decreased model accuracies in the two models that used LiDAR alone versus LiDAR and multispectral imagery combined: LiDAR only model accuracies were 82% and 86%, LiDAR and multispectral imagery combined accuracies decreased to 80% and 78% corresponding. However, this is likely less indicative of the usefulness of combining multispectral imagery data with LiDAR, as this has been shown by numerous other studies to typically increase accuracy (Hartling et al., 2021; Quan et al., 2023; Wang et al., 2023), and is likely more a reflection of the low sample sizes for the LiDAR and multispectral imagery combined data. These LiDAR and multispectral imagery combined models have an asterisk (*) symbol next to the accuracy and ROC-AUC results in Table 2 due to increased uncertainty in those results. Because of the required successional filtering of trees for these models (only 2023 trees, only trees above 20 or 30 cm due to the multispectral imagery shadow effect, only trees from one study area) the sample size of the total observations used for the model were particularly small (approximately 157 trees for the OESF area and 94 trees for the ONF area). Likely because of this, the model accuracy results varied greatly based on how the data was grouped in the training/testing split.

This is a known limitation of performing the testing/training split with smaller sample sizes—if there are trees with a unique set of characteristics that happen to all be grouped in the testing data and not the training data, the model is not trained on those characteristics, and will perform poorly when applied to the testing data. To explore the magnitude of this effect for these models, different random splits were tried, and model accuracy varied with a range of 15%. One potential solution would be to use all the data to train the model instead of performing the 75/25 data split, and to use LOOCV (leave-one-out-cross-validation) to determine accuracy (Wong, 2015). While not used here, this is a methodology recommended on smaller sample sizes as it avoids the potential split problem described above, as is a method that can be explored more using this data in future research. Overall, these LiDAR and multispectral imagery combined models should be applied sparingly and understanding of their greater uncertainty, and the final accuracies should not be used as concrete evidence that adding multispectral imagery to LiDAR models decreases model accuracy.

Model accuracies either improved or stayed the same when the top 3 m of the LiDAR trees were used (accuracies 79%, 86%, 76%, 92%, and 80%) compared to the full small cylinder (corresponding accuracies 78%, 82%, 73%, 92%, and 78%). This is likely due to the fact that most of the western redcedar trees in the OESF area were slightly shorter than their neighboring trees, leading to less LiDAR point penetration into the canopy and many cedar trees not receiving a full LiDAR profile. Thus, when combined with cedar trees that did achieve a full LiDAR point cloud profile, the height-related LiDAR metrics from the partial profile cedar trees confounded the modeling, which was avoided when only the top 3 m of the LiDAR trees were used. The one model wherein the full cylinder clip performed the same as the top 3 m clip in accuracy was for the ONF area only model. This makes sense as, due to the relative height of

cedar trees at that study area and the open conditions, most western redcedar trees from that

study area received a full LiDAR point cloud profile. Thus, depending on the individual study

area and species conditions, either a full cylinder clip or a top 3 m clip may perform better, but,

generally, a top 3 m clip appears to be a good default.

In addition to the accuracy and ROC-AUC numbers for each model, the results of the

tuned hyperparameters 'mtry' and 'min_n' are reported in Table 3 below. Typically, the optimal

number of predictors used at each decision tree node were either one or four, and the average

optimal minimum number of observations required to perform another split was 12.

Table 3. List of models and their corresponding final tuned values for hyperparameters 'mtry' (number of predictors used at each decision tree node) and 'min_n' (minimum number of observations required to perform another split)

	Model	mtry	min_n
LiDAR only	Both areas, small cylinder	1	10
	Both areas, top 3 m	4	26
	OESF area only, small cylinder	2	12
	OESF area only, top 3 m	1	7
LiDAR and multispectral imagery	Both areas, top 3 m	4	30
	Both areas, small cylinder	1	5
	ONF area only, top 3 m*	1	5
	ONF area only, small cylinder*	1	5
	OESF area only, top 3 m*	4	15
	OESF area only, small cylinder*	1	1

Finally, the top five uncorrelated predictors for each model varied greatly depending on

the model specifications and are listed in Table 4 below. All LiDAR only models used a

combination of height metrics and mean intensity (the only intensity-related metric for those

models; see Appendix C for details). The OESF multispectral imagery/LiDAR models used

more, and different, multispectral imagery metrics compared to the ONF multispectral

imagery/LiDAR models (blue and red and red-edge CI vs. only NDVI). This is further evidence

of significant differences between the study areas.

Table 4. List of models and corresponding top five predictors used for each model. Full list of predictor acronyms and meanings can be found in Appendices A and B

Model		Top 5 Predictors
LiDAR only	Both areas, small cylinder	Elev.P99, Elev.P05, Elev.IQ, Int.mean, Elev.L4
	Both areas, top 3 m	Int.mean, RP40, RP90, RP70, RP95
	OESF area only, small cylinder	Elev.P99, Int.mean, Elev.L4, Elev.L.skewness, Elev.MAD.mode
	OESF area only, top 3 m	Int.mean, Elev.skewness, Elev.CURT.mean.CUBE, RP90, Elev.P95
LiDAR and multispectral imagery	Both areas, top 3 m	Elev.P99, RP40, NDVI, RP10, RP80
	Both areas, small cylinder	Elev.P99, Int.L.CV, Elev.MAD.mode, Elev.L.skewness, RP80
	ONF area only, top 3 m*	NDVI, Int.minimum, Int.P20, Int.L.CV, Int.P01
	ONF area only, small cylinder*	Int.skewness, NDVI, Elev.P50, Int.L.CV, Elev.IQ
	OESF area only, top 3 m*	RP50, blue, RP75, RP10, red and red-edge CI
	OESF area only, small cylinder*	Elev.L.skewness, blue, Elev.P90, red and red-edge CI, RP90

Several of the models used predictors related to upper height percentiles Elev.P99,

Elev.P95, Elev.P90, and Elev.P80 (Table 4), causing concerns that these models were

distinguishing cedars based on the height differences between the cedars and surrounding trees,

ultimately making less generalizable models. This issue was investigated further: a few models

were pulled and tested without those upper percentiles, and their results were compared. For the

LiDAR only, small cylinder, OESF site only model, Elev.P99 was the top predictor in the

original model with an accuracy of 86%. Removing the top percentiles increased accuracy by a

marginal 0.5%, and interestingly the top predictors were relatively similar to the original model:

Elev.P75 instead of Elev.P95, Elev.P01 and RP90 replaced Elev.L.skewness and Elev.L4, and

Int.mean and Elev.MAD.mode maintained as top predictors. For another model, the LiDAR

only, OESF only, top 3 m model wherein Elev.P99 was the last predictor in terms of importance,

the accuracy decreased from 86% to 85% and all of the predictors stayed the same except

Elev.L.CV replaced Elev.P99 as the least important predictor. Finally, for the lidar and

multispectral model for both areas, top 3 m only, Elev.P99 was a top predictor in the original

model and when the upper percentiles were removed the model decreased from 76% to 73%,

demonstrating the greatest change in accuracy when the upper percentiles were removed.

However, the top predictors stayed relatively similar: MSR replaced NVDI, RP70 replaced

RP80, and Elev.variance became a top predictor. Overall, these results indicate that the Random

Forest algorithms may be picking up on the height differences between cedars and surrounding

trees for modeling, but, if so, differences are small enough to have relatively little impact on

overall model accuracies and top predictors.

Final maps based on the models show great promise in individual cedar tree mapping.

Models were used to predict western redcedar locations across the 2021 and 2023 LiDAR

(example in Figure 14) coverage or the coverage of the 2023 LiDAR and multispectral imagery

combined (example in Figure 15), depending on the model in question

Figure 14. Example of results mapping predicted western redcedar tree locations. Coordinates are in NAD83 / UTM zone 10N. Each individual tree is indicated by a dot which is colored based on the predicted species: "Other" in grey and "THPL" (western redcedar) in orange. This is an example using a portion of the 2021 drone LiDAR coverage and the following model: OESF only, top 3 m, 2021 and 2023 data, LiDAR only.
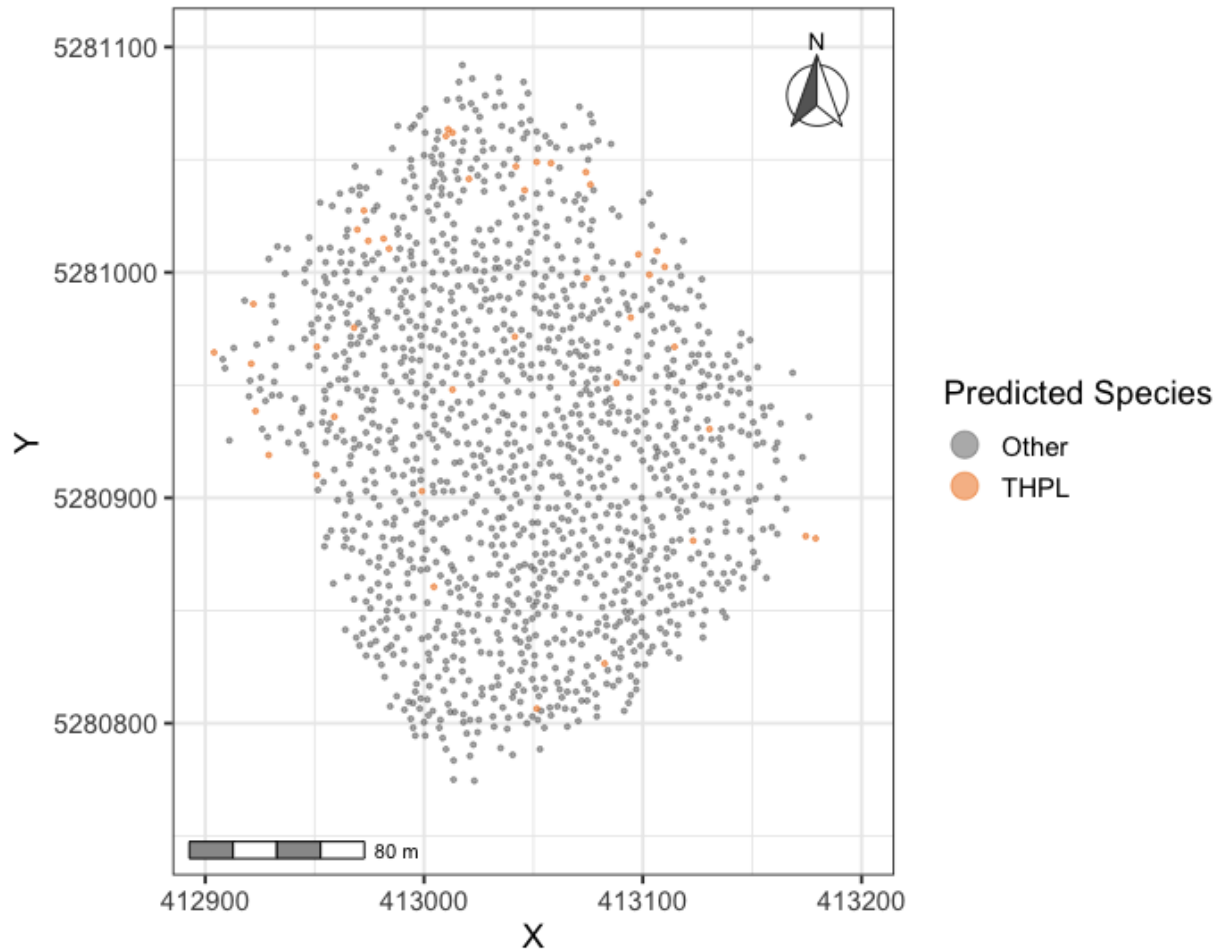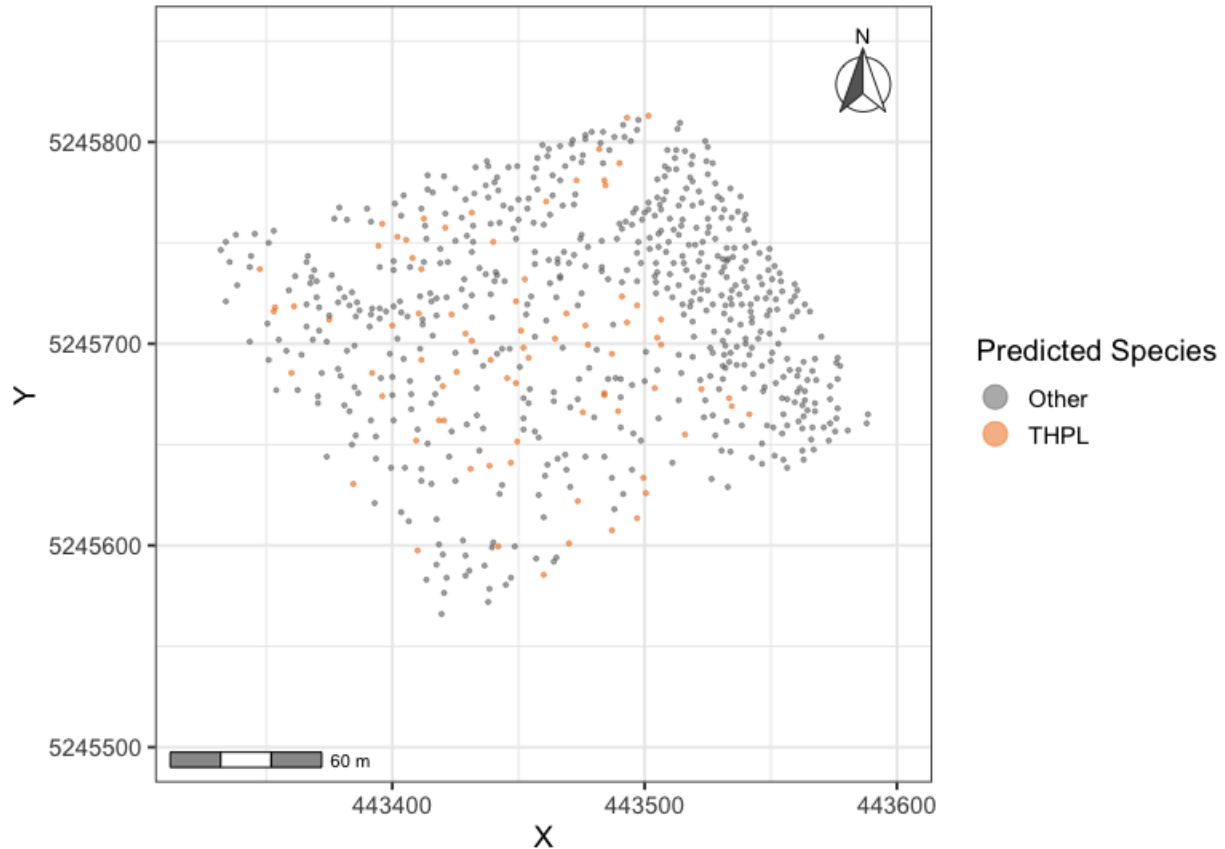
Figure 15. Example of results mapping predicted western redcedar tree locations. Coordinates are in NAD83 / UTM zone 10N. Each individual tree is indicated by a dot which is colored based on the predicted species: "Other" in grey and "THPL" (western redcedar) in orange. This is an example using a portion of the 2022 drone LiDAR and multispectral imagery coverage and the following model: ONF only, top 3 m, 2023 data only, LiDAR and multispectral imagery combined.

3.2. Analysis Using Multispectral Imagery as a Proxy for Western Redcedar Health

A preliminary exploratory analysis of the multispectral imagery metrics data revealed key age/study area differences between the ONF and OESF areas (Figure 16). The magnitude of these differences depended on the multispectral imagery metrics in question (Figure 16). Regardless, sufficient differences were observed to warrant a more formal comparison and analysis.
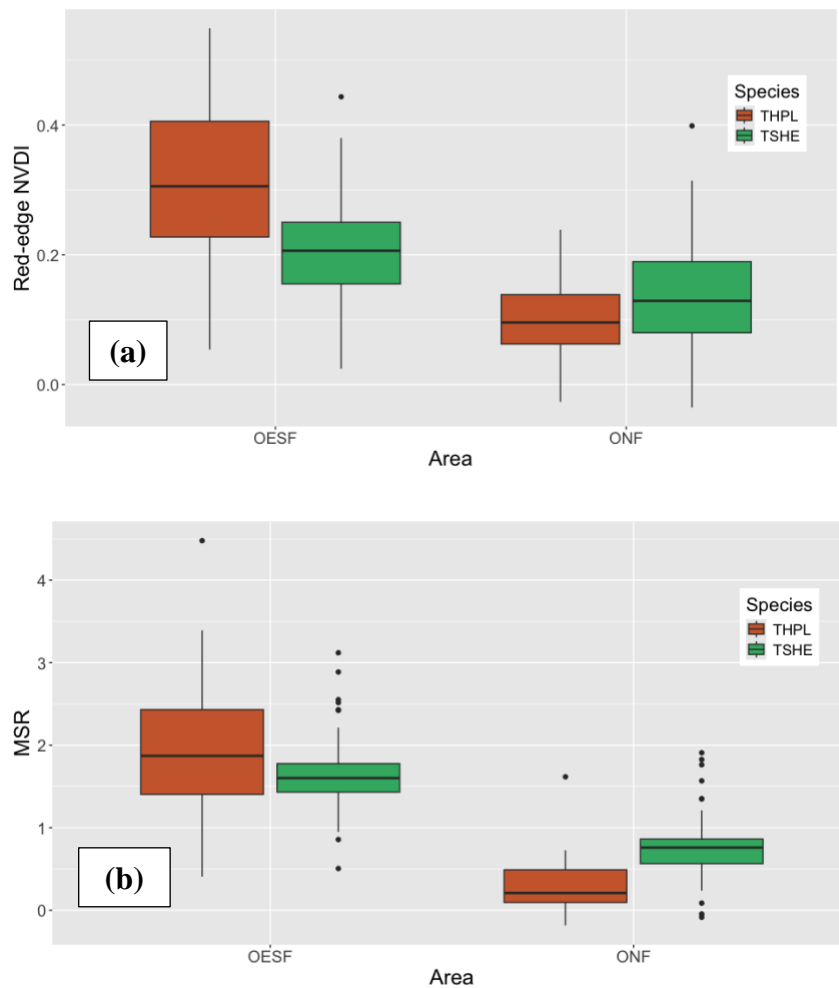
Figure 16. Boxplots comparing differences in multispectral imagery metrics (using examples of red-edge NVDI **(a)** and MSR **(b)**; see Appendix B for multispectral indices list and meanings) across study areas (OESF and ONF) and species. Species are colored with western hemlocks ("TSHE") as green and western redcedar ("THPL") as brown.

This more formal analysis and comparison took the form of a principal component analysis (PCA). The first two components explained the majority of the variance in the dataset, with 89% of the variance explained between the first two axes. The magnitude of the loadings for each multispectral imagery metric were relatively similar for the first principal component,

indicating that all the multispectral imagery metrics had a similar level of influence over the

analysis results. The PCA was graphed to determine any visual patterns (Figure 17).
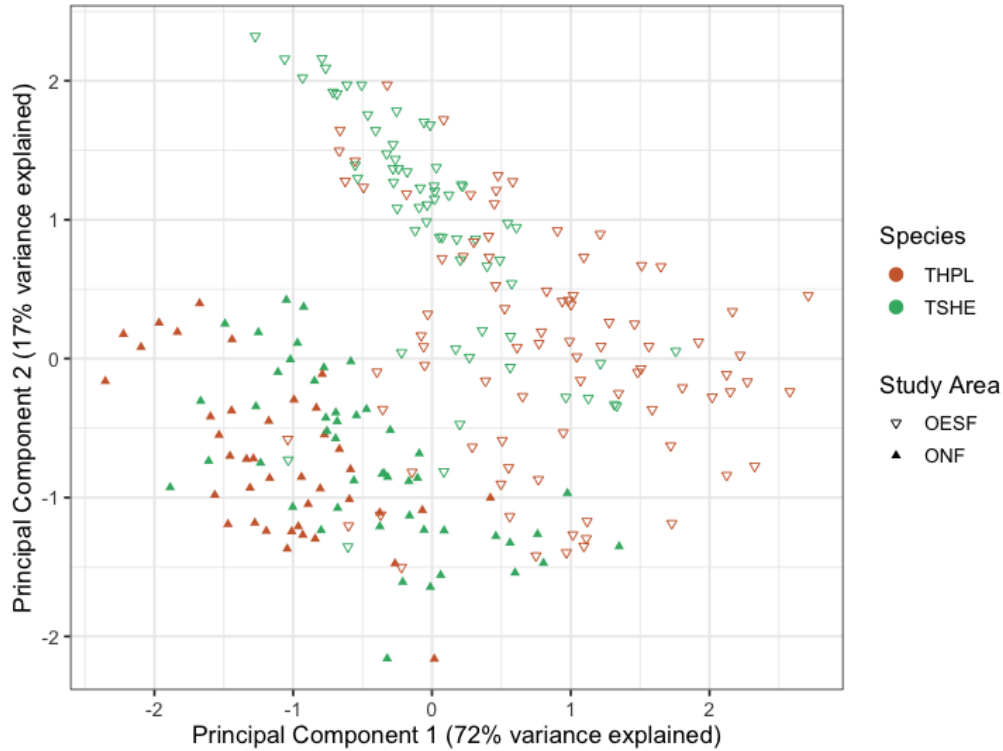
Figure 17. First two principal components of the PCA graphed. Individual trees are shaped based on study area (OESF indicated by the unfilled upside-down triangles, and ONF indicated by the filled right-side-up triangles) and colored based on species (western redcedar ("THPL") in brown and western hemlock ("TSHE") in green). The two axis labels include how much model variance was explained by each of the first two principal components.

Two patterns were observed in the graphed PCA: 1) study area/age appeared to be

correlated with the second principal component; and 2) species appeared to be correlated with

the first principal component, with western redcedar appearing on either side of the western

hemlock trees depending on study area. This is a pattern that was reflected in the original boxplot

exploratory analysis—the relationship between western hemlock metrics and western redcedar

metrics flips depending on study area. To confirm that species and study area were indeed

45

correlated with the first and second principal components respectively, ANOVA tests were

subsequently performed. The ANOVA for the second principal component scores vs. study area

were significant with a p-value less than 0.05 and explained 37% of the variance (Figure 18).
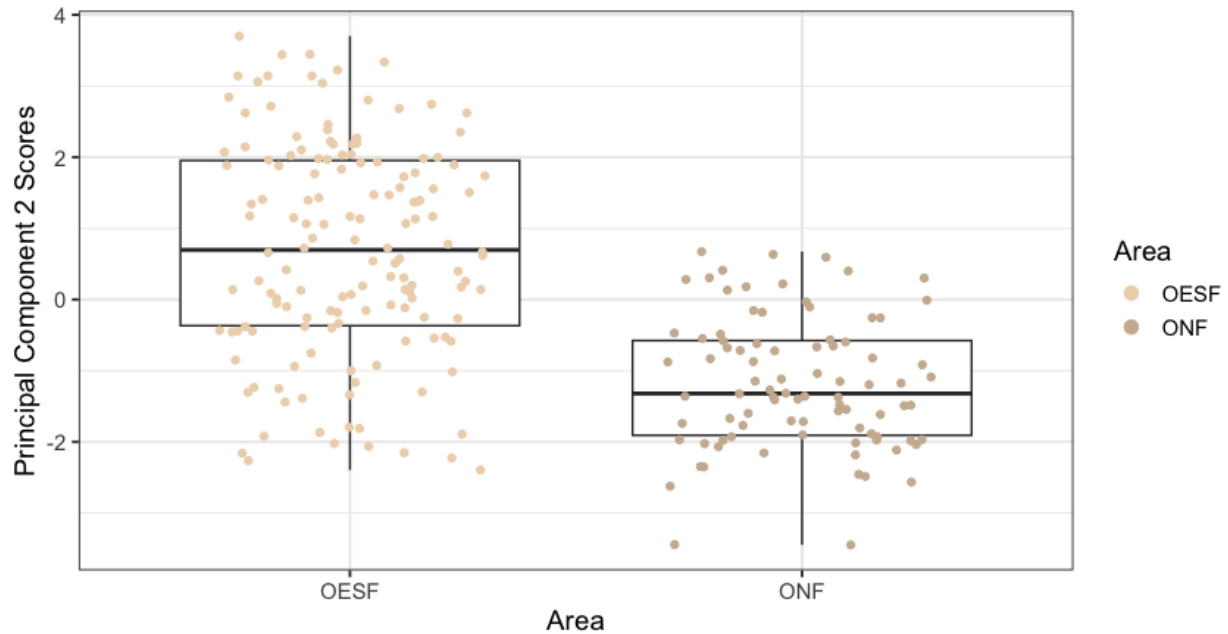
Figure 18. Boxplot of the second principal component scores comparatively between the two study areas OESF and ONF. Model observations (multispectral imagery metrics associated with individual trees) are indicated via dots that are additionally colored by study area (light brown for OESF, dark brown for ONF).

The ANOVA for the first principal component scores vs. species had a significant p-

value of less than 0.05, but only explained 2% of the variance. However, this was expected due

to the divergent nature of the study areas in terms of the relationships between western redcedar

and western hemlock within in each area. Thus, the two study areas were subset and

subsequently each compared to the first principal component (Figure 19). Both ANOVAs

resulted in a significant p-value of less than 0.05. The ONF area ANOVA explained 26% of the

variance and the OESF area explained 12% of the variance, for a combined 38% of variance

explained, indicating that species does indeed appear related to the first principal component.

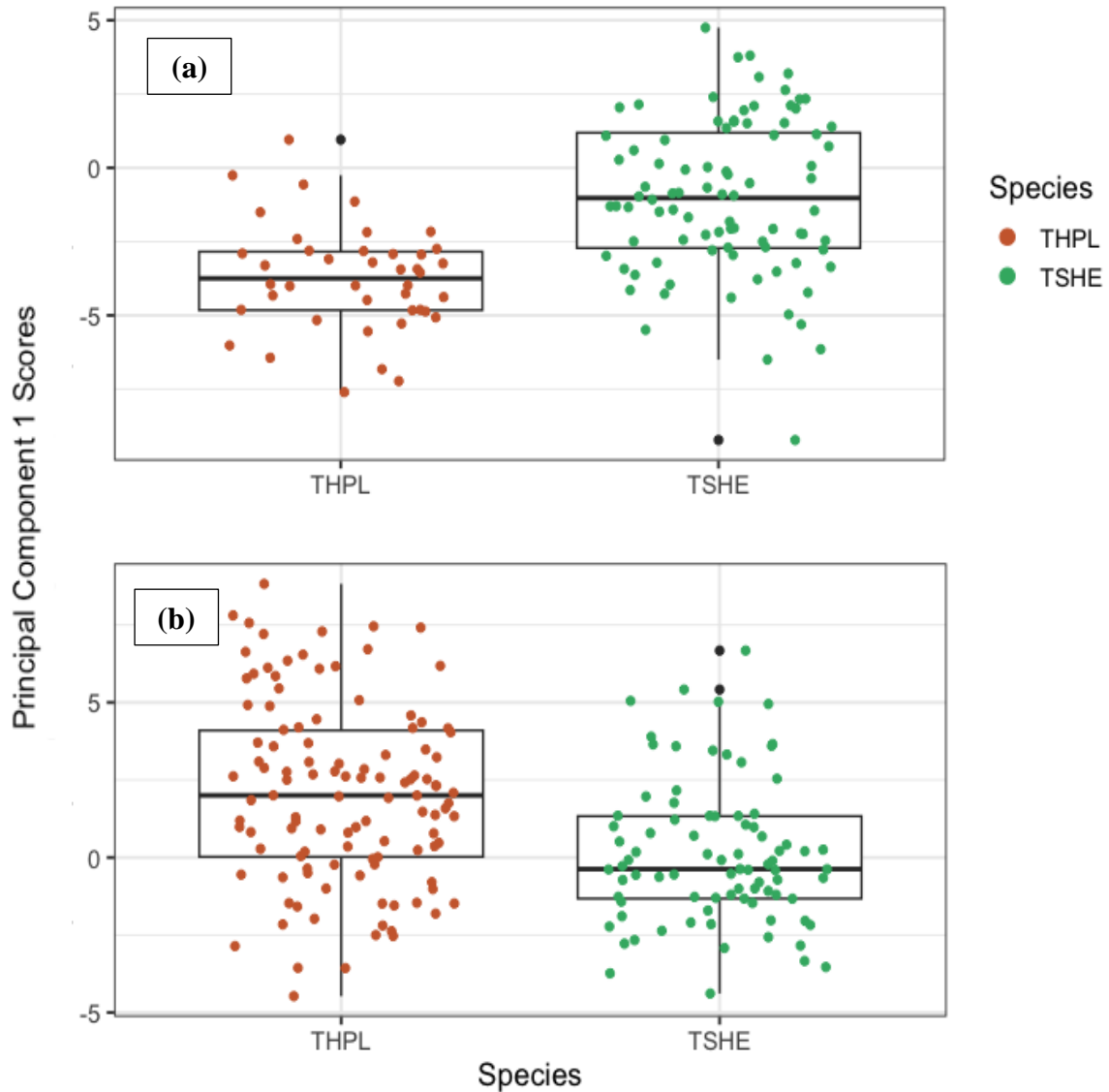**Figure 19**. Boxplots of the first principal component scores comparatively between species, separated by study area: the ONF area **(a)** and the OESF area **(b)**. Model observations (multispectral imagery metrics associated with individual trees) are indicated via dots that are additionally colored by species (brown for western redcedar ("THPL"), green for western hemlock ("TSHE")).

Overall, these analyses indicate strong study area differences and strong species differences within those study areas across the multispectral imagery metrics.

4. Discussion

4.1. LiDAR and Multispectral Imagery Models for Classifying and Mapping Western Redcedars

For this study, ten models predicting western redcedar locations were performed. Model accuracies ranged from 73-92% depending on the model in question, with the more stable model accuracies ranging from 78-86% (see section 3.1. for discussion on the variability of the accuracies for the multispectral imagery/LiDAR combined models). Classification accuracies typically vary depending on the remote sensing data used, the number of classifiers (species), the algorithm used, and the magnitude of geomorphic and/or physiological differences between species classified (ex. classifying two deciduous trees or a deciduous tree vs. an evergreen tree). Based on a review study that looked at 129 different cases of species classifications using remote sensing, including 17 LiDAR only models and 28 combined models, accuracies of 78 to 86% fall within the interquartile range of other study accuracies, and the 86% accuracy is on the higher end of the range for a LiDAR only model (Fassnacht et al., 2016). Only one study that classified western redcedar trees specifically was found for comparison: a study in Seattle using airborne LiDAR was able to classify five different species, including western redcedar, with an overall accuracy of 85% (Vaughn et al., 2012). That accuracy is only slightly smaller than the best accuracy achieved in this study (86%), likely because it used a more restricted dataset using data from the University of Washington Arboretum and only 27 western redcedar trees total (Vaughn et al., 2012).

Part of this study was to create the optimal model for western redcedar tree species classification within the T3 Experiment and to better understand the biogeography of western redcedars—their distribution and factors controlling that distribution. This was determined to be the model that used the 2021 and 2023 data combined, the top 3 m of the LiDAR trees only, only the LiDAR data, only data from the OESF. The model accuracy for this model was 86% with an ROC-AUC score of 94%.

Similarly to the multispectral imagery spectral signatures analysis, large study area differences were observed in the results of the LiDAR classification modeling. Due to these significant study area/age effects, future research should either plan to subset by study area as part of the methodology or collect more data to be able to incorporate study area differences more fully into the model. Models will likely always benefit when subset by geographic position, age, or other factors, as that narrows the training data conditions, but more data could help alleviate the confounding effects of such differences. For the models created in this research, the models should only be applied to areas of similar forest composition and structure (i.e. for the OESF area, 40- to 70-year-old managed second-growth stands of primarily western hemlock and Douglas-fir, and for the ONF area, approximately 200-years-old or more stands of primarily western hemlock and western redcedar).

4.2. Multispectral Imagery as Proxy for Cedar Health Analysis

Trees in the two study areas of different ages and sizes had markedly different multispectral signatures, precluding development of a generalized model. Specifically, the relationship between mean western redcedar and mean western hemlock values reverse based on study area—for the ONF area the western redcedars typically had lower metric values compared

to western hemlocks; for the OESF area the western redcedars typically had higher values compared to the western hemlocks. There are many different possible explanations for this phenomenon; spectral differences could be indicating crown stress caused by underlying health issues, or they may not—there are many uncertainties surrounding what is driving these differences that are discussed in this section.

There is the possibility that these signature differences were not driven by the trees themselves, but rather the multispectral imagery itself as the two study areas were flown on different days. Multispectral imagery can be influenced by seasonal and weather conditions, as well as meteorological conditions (Kedzierski et al., 2019). This is important to highlight as it is a very real effect. However, this is unlikely to be the case for this study. Although the two study areas were flown on different days, they were flown only a week apart and during the same time of day between 11 am and 1 pm. The two study areas were additionally flown under similar weather conditions: a weather station based in Forks, WA, near the OESF area recorded a mean temperature at the time of the flights of 24.6 ℃, relative humidity mean percent of 47%, and 0.00 total precipitation (*Forks Washington RAWS Data*, n.d.). A weather station outside of Humptulips, WA, near the ONF area recorded a mean temperature at the time of flights of 19.4 ℃, relative humidity mean percent of 53%, and 0.00 total precipitation (*Black Knob Washington RAWS Data*, n.d.). Furthermore, the multispectral imagery camera used for these flights was equipped with a light meter and reflectance panel that were used to calibrate the images. Thus, while it is a valid concern worth considering, it is unlikely that it is the multispectral imagery itself driving these differences, particularly to the extent of which the differences were observed.

If the multispectral imagery itself is not causing these differences, there are other possible explanations. The first is that the multispectral signatures are indicating crown stress that appears

in the ONF cedars but not the OESF cedars. This is supported by the fact that seven of the ONF cedars had dead tops that were noted during the LiDAR matching process, whereas no dead tops were found on the OESF cedars. One possible explanation for why the well-established ONF cedars could be experiences more crown stress compared to the younger OESF cedars comes from a recent study on the cedar dieback phenomenon. They noted that oftentimes healthy cedars—indicated by the color and fullness of the cedar leaves—could be found near unhealthy cedars, and the distinguishing factor seemed to be that the healthy cedars were shaded by nearby canopies, whereas the unhealthy cedars were more exposed (Betsy Goodrich et al., 2023). They hypothesized that the unhealthy cedars that were more exposed had increased sunlight and wind exposure, the combination of which exacerbated drought stress (Betsy Goodrich et al., 2023). This could be what is occurring at the ONF vs. OESF study areas as well—the cedars in the ONF area are typically the tallest trees and are in a much more open canopy, leading to significantly more exposure than the OESF cedars, and ultimately increased indicators of crown stress.

However, there are several other explanations as well, related to differences in age, height, and growing conditions between the study areas. One study focused on Douglas-fir trees found morphological differences between the needles of Douglas-fir saplings and old-growth trees; in particular, they found that old-growth tree needles had an average of 11% less photosynthetic mesophyll area compared to sapling needles (Apple et al., 2002). If this is true with western redcedar trees as well, the differences in the multispectral imagery metrics could be driven by the fact that older tree needles photosynthesize less, and not an indication of crown stress or potential underlying health issues. Perhaps it's based on height limitations on water availability as seen in redwoods (*Sequoia sempervirens*) where taller trees tend to have increased leaf water stress due to the impacts of gravity that can lead to reduced photosynthesis (Koch et

al., 2004). This is another example of an explanation tied to the demographics of the western redcedar in the ONF.

Alternatively, the differences may be caused by differences in the soil of the study areas: cedars that grow in wetter conditions tend to have shallower roots, and thus have less access to water during dry years, ultimately leading to insufficient water transport to the top of the tree—the area of the tree visible by the multispectral imagery (C. Harrington, personal communication, May 2, 2024). Thus, even assuming that the multispectral signature differences are indicating crown stress, this may be a standard phenomenon for cedars trees in those conditions, and not an indication of underlying health issues. Furthermore, there may be other underlying factors such as mechanical damages (Larson & Franklin, 2010) and biotic agents (Das et al., 2016) that regularly play roles in forest ecosystems, and often act in nuanced and unpredictable ways (Franklin et al., 1987).

Ultimately, there are too many confounding factors to determine a final cause of these study area differences. More data, from several different study areas with different conditions recorded in-depth, are needed before firm conclusions can be drawn. What has been discussed here should be used as a starting point for future methodologies, particularly when deciding study area(s) and ground measurements.

4.3. Future Research Recommendations

The models described in this study, in particular the OESF only, 2021 and 2023 data, top 3 m, LiDAR only model, shows potential for model expansion from the smaller spatial coverage of the UAV LiDAR to larger airborne LiDAR. Up-scaling remote sensing data in this way has been used by others (i.e. Margolis et al., 2015) to regionalize remote sensing models. Essentially,

the western redcedar trees identified by the UAV LiDAR model would be used to train a plane-based airborne LiDAR model to identify and map western redcedar trees over a larger area, starting with the 20,000 acres of the T3 Watershed Experiment. Further expansion could follow to areas of interest to the Quileute Tribe Natural Resources Department. Trees identified by the UAV LiDAR model could be subset to only include trees wherein 70% or more of the Random Forest decision trees identified the LiDAR tree as western redcedar, increasing overall model accuracy. The spatial extent of the model would be limited to forested areas of similar age, composition, and structure of that of the training dataset, as deviating too far from the training dataset could greatly reduce model accuracy. That said, this shows great promise for a more regional model of larger spatial coverage.

Furthermore, with these cedar maps and the potential for maps of a larger spatial coverage, there is the opportunity to tie current western redcedar locations to other environmental factors and study area conditions—learning more about cedar's biogeography. The following variables could be mapped against cedar abundance to determine ideals conditions for cedar growth: elevation, slope, aspect, soil type, water moisture, and more. Maps of individual western redcedar tree locations unlock the possibility of many such studies.

Additionally, further work could include a more formal analysis of the social and collaborative aspects of this work. This could include how this work has aligned with past collaborative work and how it falls within the framework of social and collaborative learning. It could also include more formalized surveys or interviews with the purpose of creating a deeper understanding of cedar's cultural and economic importance for local community members. These surveys/interviews would then inform future work that could be even more tailored to local community needs.

5. Conclusion

This research demonstrates a robust methodology to create Random Forest models trained on UAV LiDAR with or without multispectral imagery to classify and map western redcedar trees on an individual tree level basis. These models are important due to the great cultural, economic, and ecological impacts of western redcedars trees, particularly with the decreased abundance of cedar trees across the landscape. Maps from these models can be used for pre-treatment assessments of the T3 Experiment, researching the biogeography of western redcedar, and for tribal purposes by the Quileute Natural Resources Department. This research found that the optimal models for classifying cedar were subset based on study area/age and used only the top 3 m—as opposed to a full cylinder—of the LiDAR point clouds for individual trees; using these specifications, a model of accuracy 86% was achieved.

Additionally, there is great potential for using multispectral imagery metrics as proxies/indicators of western redcedar health; however, there are many confounding factors that need to be considered first, such as the impact of tree age and other standard biological processes on multispectral imagery metrics.

Acknowledgements

There are too many to thank here for help and support on my master's thesis. Thank you to my committee members Bernard Bormann, Bob McGaughey, and Marc Miller. A huge thank you to Courtney Bobsin; graduate school would have looked extremely different without your support. Thank you to my amazing ONRC summer interns who participated in the great 2023 cedar hunt with me: Paisley Blume, Nina Perry, Anna Thario, Jovanna Talarico, and Evan Gray. Thank you as well to the amazing 2021 ONRC summer interns who collected the 2021 data used in this project. Thank you to all of the amazing ONRC staff who have supported this work over the years: Deric Kettle, Theresa Santman, Jordan Sallee, Gia Gallina, Keven Bennett, and Renee Reed. Thank you to Chris Erickson for flying and processing the LiDAR and multispectral imagery data, and for working with us throughout this project. Thank you to the Quileute Tribe Natural Resources Department, specifically Garrett Rasmussen and Chris Terry, for partnering with us on this project. Thank you to all the members of the T3 Cedar Learning Group for their feedback and expertise, including Connie Harrington for your continued support and advice. Thank you to all of the Washington State Department of Natural Resources employees who have supported this project work and the work in the T3 Watershed Experiment in general; shout out to Teddy Minkova, Tracy Petroske, and Emily Gardner for your supreme leadership and organization skills. Thank you to the Olympic National Forest for working with us and allowing us to take measurements on national forest land. And finally, thank you to all my friends and family who have supported me throughout this thesis and graduate school experience, I truly could not have done it without you.

Appendix A. LiDAR Metrics Acronyms and Meanings

LiDAR metrics used in modeling were cloud metrics computed by FUSION software, with the exception of the relative percentiles, which were computed by dividing each elevation percentile by the 99th elevation percentile. See FUSION manual for cloud metric specifications and equations (McGaughey, 2023b). Variables that were used in all models are indicated with an asterisk (*), variables that were used in the 2023 data only models are indicated with a dot (•). All other variables were computed as cloud metrics but were dropped for the model making. Note that these metrics were run on normalized point clouds—thus, the elevation variables can be thought of as height-related variables.

Variable Name	What it stands for
Total.return.count	Total number of LiDAR returns
Return.1.count, Return.2.count, Return.3.count, Return.4.count, Return.5.count, Return.6.count, Return.7.count, Return.8.count, Return.9.count	LiDAR return counts
Other.return.count	Number of returns that don't fall into any above category
Elev.minimum	Minimum elevation
Elev.maximum	Maximum elevation
Elev.mean *	Mean elevation
Elev.mode *	Mode elevation
Elev.stddev *	Standard deviation of elevation
Elev.variance *	Elevation variance
Elev.CV *	Coefficient of variation for elevation
Elev.IQ *	Interquartile distance for elevation
Elev.skewness *	Elevation skewness
Elev.kurtosis *	Elevation kurtosis
Elev.AAD *	Average absolute deviation for Elevation
Elev.MAD.median *	Median absolute deviation from the median for Elevation
Elev.MAD.mode *	Median absolute deviation from the mode for Elevation
Elev.L1 *	First L moment for Elevation
Elev.L2 *	Second L moment for Elevation
Elev.L3 *	Third L moment for Elevation

Elev.L4 *	Fourth L moment for Elevation
Elev.L.CV*	L moment coefficient of variance for elevation
Elev.L.skewness *	L moment skewness for elevation
Elev.L.kurtosis *	L moment kurtosis for elevation
Elev.P01, Elev.P05, Elev.P10, Elev.P20 , Elev.P25, Elev.P30, Elev.P40, Elev.P50, Elev.P60, Elev.P70, Elev.P75, Elev.P80, Elev.P90, Elev.P95, Elev.P99 *(all)	Elevation percentiles
Canopy.relief.ratio *	Canopy relief ratio
Elev.SQRT.mean.SQ *	Generalized mean for the 2nd power for elevation
Elev.CURT.mean.CUBE *	Generalized mean for the 3rd power for elevation
Int.minimum •	Intensity minimum
Int.maximum •	Intensity maximum
Int.mean *	Intensity mean
Int.mode •	Intensity mode
Int.stddev •	Standard deviation for intensity
Int.variance •	Intensity variance
Int.CV •	Coefficient of variance for intensity
Int.IQ •	Interquartile distance for intensity
Int.skewness •	Intensity skewness
Int.kurtosis •	Intensity kurtosis
Int.AAD •	Average absolute deviation for intensity
Int.L1 •	First L moment for intensity
Int.L2 •	Second L moment for intensity
Int.L3 •	Third L moment for intensity
Int.L4 •	Fourth L momen for intensity
Int.L.CV •	L moment coefficient of variance
Int.L.skewness •	L moment skewness
Int.L.kurtosis •	L moment kurtosis
Int.P01, Int.P05, Int.P10, Int.P20, Int.P25, Int.P30, Int.P40, Int.P50, Int.P60, Int.P70, Int.P75, Int.P80, Int.P90, Int.P95, Int.P99 •(all)	Intensity percentiles
Profile.area *	Profile area
RP01, RP05, RP10, RP20, RP25, RP30, RP40, RP50, RP60, RP70, RP75, RP80, RP90, RP95 *	Relative percentiles

Appendix B. Multispectral Imagery Bands and Indices

Multispectral imagery metrics were derived from multispectral imagery bands and indices, listed below. All indices were computed using equations from Xie et. al, 2018.

Multispectral Band/Index	Where it came from
Red	Original band from AgEagle Altum-PT sensor
green	Original band from AgEagle Altum-PT sensor
blue	Original band from AgEagle Altum-PT sensor
near-infrared (NIR)	Original band from AgEagle Altum-PT sensor
red-edge (between red and NIR)	Original band from AgEagle Altum-PT sensor
green chlorophyll index (CI)	$(\frac{NIR}{green}) - 1$
red-edge CI	$(\frac{NIR}{red-edge}) - 1$
red and red-edge CI	$\frac{NIR}{0.4 \times red + (1 - 0.4) \times red\text{–}edge} - 1$
modified simple ratio (MSR)	$\frac{(\frac{NIR}{red}) - 1}{\sqrt{(\frac{NIR}{red}) + 1}}$
red-edge MSR	$\frac{(\frac{NIR}{red-edge}) - 1}{\sqrt{(\frac{NIR}{red-edge}) + 1}}$
red and red-edge MSR	$\frac{\left(\frac{NIR}{0.4 \times red + (1 - 0.4) \times red\text{–}edge}\right) - 1}{\sqrt{\left(\frac{NIR}{0.4 \times red + (1 - 0.4) \times red\text{–}edge}\right) + 1}}$
normalized difference vegetation index (NDVI)	$\frac{NIR - red}{NIR + red}$
red-edge NDVI	$\frac{NIR - red\text{–}edge}{NIR + red\text{–}edge}$

red and red-edge NDVI	$$\frac{NIR - (0.4 \times red + (1 - 0.4) \times red\text{-}edge)}{NIR + (0.4 \times red + (1 - 0.4) \times red\text{-}edge)}$$

Appendix C. LiDAR Intensity Correction for 2021/2023 Data

The LiDAR intensity values for the 2021 and 2023 data were generated by two different sensors and greatly differ, both in terms of the magnitude and range of values (Figure 20). The need for LiDAR intensity correction/calibration/normalization is a known problem within the field, one with no standardized solution (Kashani et al., 2015). The following is what was determined to be the best solution for the purpose of this research study.
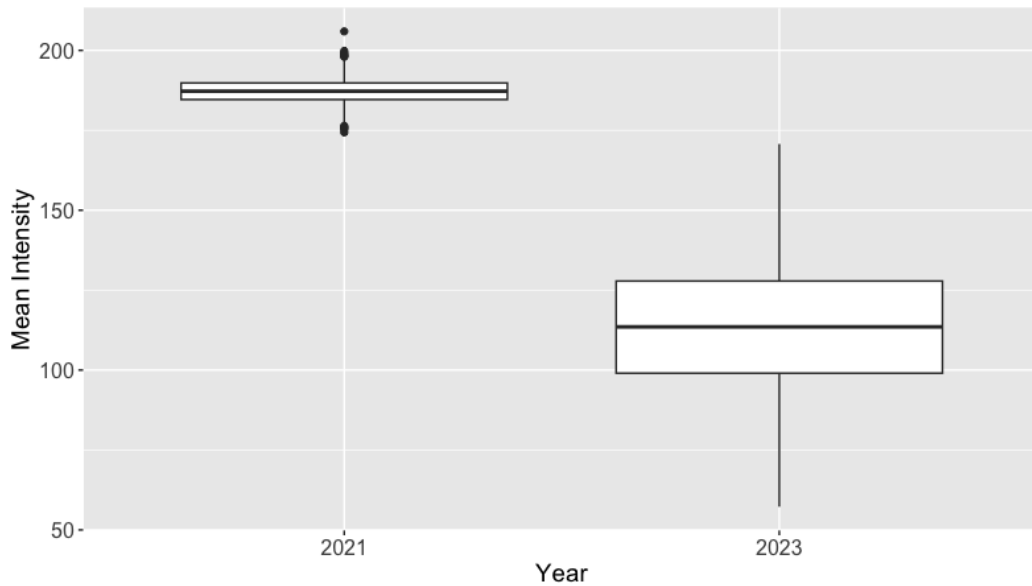

Figure 20. Boxplots of mean intensity values from every LiDAR point used in modeling separated by data collection year.

First, cloud metrics were run (using FUSION version 4.51) on all the LiDAR point clouds from the years 2021 and 2023 separately. These cloud metrics were computed using the first returns only, as those are typically the most stable returns, and only returns above 2 m to avoid ground points. Two cloud metrics that resulted were mean intensity and standard deviation for each LiDAR point cloud file. The mean intensities and standard deviations for all the point

clouds within each year were averaged to determine a mean intensity and standard deviation for each year. These were then used in a z-score normalization on every intensity value from every LiDAR point cloud used in modeling. A z-score normalization was picked because the mean intensity values appeared to be relatively normal in distribution, and due to its relatively robust handling of outliers.

Unfortunately, due to species quantities limitations between years (Figure 5), the only species with a sufficient sample size to compare intensity values between the two years was western hemlock. Thus, after the correction was applied, a boxplot comparing the intensity values for western hemlocks within each year was created to assess the effectiveness of this intensity correction (Figure 21). Based on the boxplot result, the intensity correction appeared sufficiently effective. To further test this, the species model was run using 2023 data and western hemlocks and western redcedar only, and then run again using the 2023 and 2021 data with only western hemlocks and western redcedar, and the model accuracies were compared. The model accuracy results for these two models were identical, adding confidence to the effectiveness of the intensity correction.
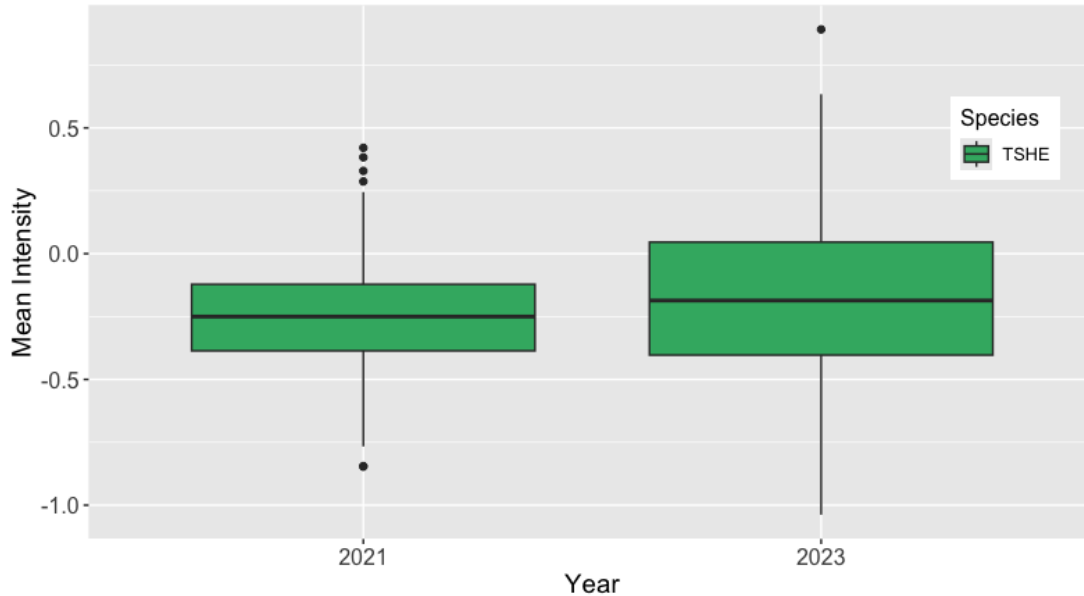
Figure 21. Boxplots of mean intensity values from every western hemlock (TSHE) LiDAR point used in modeling, separated by data collection year.

Unfortunately, this intensity correction only worked on the mean intensity values. To correct the other intensity-related metrics (percentiles, skewness, kurtosis, etc.), further research and experimentation outside of the scope of this study would be required.

References

AgEagle Altum-PT Brochure. (2022). AgEagle. https://ageagle.com/wp-content/uploads/2022/07/AgEagle-Altum-PT-Brochure-EN.pdf

Alban, D. H. (1969). The Influence of Western Hemlock and Western Redcedar on Soil Properties. Soil Science Society of America Journal, 33(3), 453–457. https://doi.org/10.2136/sssaj1969.03615995003300030033x

Andrus, R. A., Peach, L. R., Cinquini, A. R., Mills, B., Yusi, J. T., Buhl, C., Fischer, M., Goodrich, B. A., Hulbert, J. M., Holz, A., Meddens, A. J. H., Moffett, K. B., Ramirez, A., & Adams, H. D. (2023). Canary in the forest?—Tree mortality and canopy dieback of western redcedar linked to drier and warmer summers. Journal of Biogeography, 51(1), 103–119. https://doi.org/10.1111/jbi.14732

Antos, J. A., Filipescu, C. N., & Negrave, R. W. (2016). Ecology of western redcedar (Thuja plicata): Implications for management of a high-value multiple-use resource. Forest Ecology and Management, 375, 211–222. https://doi.org/10.1016/j.foreco.2016.05.043

Apple, M., Tiekotter, K., Snow, M., Young, J., Soeldner, A., Phillips, D., Tingey, D., & Bond, B. J. (2002). Needle anatomy changes with increasing tree age in Douglas-fir. Tree Physiology, 22(2–3), 129–136. https://doi.org/10.1093/treephys/22.2-3.129

Backoulou, G. F., Elliott, N. C., Giles, K., Phoofolo, M., & Catana, V. (2011). Development of a method using multispectral imagery and spatial pattern metrics to quantify stress to wheat fields caused by Diuraphis noxia. Computers and Electronics in Agriculture, 75(1), 64–70. https://doi.org/10.1016/j.compag.2010.09.011

Bakker, J. D. (2024). Applied Multivariate Statistics in R. University of Washington. https://uw.pressbooks.pub/appliedmultivariatestatistics/

Betsy Goodrich, Melissa Fischer, & Christine Buhl. (2023, April 10). Western redcedar dieback [StoryMap]. https://storymaps.arcgis.com/stories/1405dab5f59246aa83849ec43f72b15a

Bioregional Assessment of Northwest Forests. (2020). USDA Forest Service. https://www.fs.usda.gov/Internet/FSE_DOCUMENTS/fseprd762774.pdf

Black Knob Washington RAWS Data. (n.d.). RAWS USA Climate Archive. Retrieved May 14, 2024, from https://raws.dri.edu/cgi-bin/rawMAIN.pl?waWBLA

Bobsin, C. R., Bormann, B. T., Miller, M. L., & Pelach, B. D. (2023). Perspectives: Ethnoforestry, ecosystem wellbeing, and collaborative learning in the Pacific Northwest. Forest Ecology and Management, 529, 120738. https://doi.org/10.1016/j.foreco.2022.120738

Bolsinger, C. L. (1979). Western Redcedar: A Forest Resource in Transition. Department of Agriculture, Forest Service, Pacific Northwest Forest and Range Experiment Station.

Cornwell, R. (2022). Regenerating Western Redcedar Under Ungulate Browsing Pressure In the Olympic Peninsula: An Ethnoforestry Approach.

da Cunha Neto, E. M., Rex, F. E., Veras, H. F. P., Moura, M. M., Sanquetta, C. R., Käfer, P. S., Sanquetta, M. N. I., Zambrano, A. M. A., Broadbent, E. N., & Corte, A. P. D. (2021). Using high-density UAV-Lidar for deriving tree height of Araucaria Angustifolia in an Urban Atlantic Rain Forest. Urban Forestry & Urban Greening, 63, N.PAG-N.PAG. https://doi.org/10.1016/j.ufug.2021.127197

Dalponte, M., Bruzzone, L., & Gianelle, D. (2012). Tree species classification in the Southern Alps based on the fusion of very high geometrical resolution multispectral/hyperspectral images and LiDAR data. Remote Sensing of Environment, 123, 258–270. https://doi.org/10.1016/j.rse.2012.03.013

Das, A. J., Stephenson, N. L., & Davis, K. P. (2016). Why do trees die? Characterizing the drivers of background tree mortality. Ecology, 97(10), 2616–2627. https://doi.org/10.1002/ecy.1497

Dash, J. P., Pearse, G. D., & Watt, M. S. (2018). UAV Multispectral Imagery Can Complement Satellite Data for Monitoring Forest Health. Remote Sensing, 10(8), Article 8. https://doi.org/10.3390/rs10081216

DNR Strategic Plan 2022-2025. (2022). Washington State Department of Natural Resources. https://www.dnr.wa.gov/publications/em_strategic_plan_2022.pdf

Donnelly, D., Dixon, G., Dixon, C., Havis, R., Keyser, C., Rebain, S., Smith-Mateja, E., & Vandendriesche, D. (2022). Pacific Northwest Coast (PN) Variant Overview of the Forest Vegetation Simulator (p. 75). U. S. Department of Agriculture, Forest Service, Forest Management Service Center. https://www.fs.usda.gov/fmsc/ftp/fvs/docs/overviews/FVSpn_Overview.pdf

Fassnacht, F. E., Latifi, H., Stereńczak, K., Modzelewska, A., Lefsky, M., Waser, L. T., Straub, C., & Ghosh, A. (2016). Review of studies on tree species classification from remotely sensed data. Remote Sensing of Environment, 186, 64–87. https://doi.org/10.1016/j.rse.2016.08.013

Feng, B., Nie, S., Wang, C., Xi, X., Wang, J., Zhou, G., & Wang, H. (2022). Exploring the Potential of UAV LiDAR Data for Trunk Point Extraction and Direct DBH Measurement. Remote Sensing, 14(12), N.PAG-N.PAG. https://doi.org/10.3390/rs14122753

Fischer, M. J. (2019, December 4). Western Redcedar East of the Cascades: A Species in Decline? Forest Stewardship Notes. https://sflonews.wordpress.com/2019/12/04/western-redcedar-east-of-the-cascades-a-species-in-decline/

Forks Washington RAWS Data. (n.d.). RAWS USA Climate Archive. Retrieved May 14, 2024, from https://raws.dri.edu/cgi-bin/rawMAIN.pl?waWFOR

Franklin, J. F., Shugart, H. H., & Harmon, M. E. (1987). Tree Death as an Ecological Process. BioScience, 37(8), 550–556. https://doi.org/10.2307/1310665

Franklin, J. F., & Spies, T. A. (1983). CHARACTERISTICS OF OLD-GROWTH DOUGLAS-FIR FORESTS. New Forests For a Changing World. SAF National Convention. https://andrewsforest.oregonstate.edu/sites/default/files/lter/pubs/pdf/pub120.pdf

Fraser, B. T., & Congalton, R. G. (2021). Monitoring Fine-Scale Forest Health Using Unmanned Aerial Systems (UAS) Multispectral Models. Remote Sensing, 13(23), Article 23. https://doi.org/10.3390/rs13234873

Garibaldi, A., & Turner, N. (2004). Cultural Keystone Species: Implications for Ecological Conservation and Restoration. Ecology and Society, 9(3), art1. https://doi.org/10.5751/ES-00669-090301

Gong, Y., Li, X., Du, H., Zhou, G., Mao, F., Zhou, L., Zhang, B., Xuan, J., & Zhu, D. (2023). Tree Species Classifications of Urban Forests Using UAV-LiDAR Intensity Frequency Data. Remote Sensing, 15(1), 110. https://doi.org/10.3390/rs15010110

Gordon, J., Sessions, J., Bailey, J., Cleaves, D., Corrao, V., Leighton, A., Mason, L., Rasmussen, M., Salwasser, H., & Sterner, M. (2013). Assessment of Indian Forests and Forest Management in the United States: Executive Summary. Indian Forest Management Assessment Team for the Intertribal Timber Council. http://www.itcnet.org/issues_projects/issues_2/forest_management/assessment.html

Gregory, C., McBeath, A., & Filipescu, C. (2018). An Economic Assessment of the Western Redcedar Industry in British Columbia (Information Report FI-X-017). Canadian Forest Service, Natural Resources Canada.

Gunther, E. (1973). Ethnobotany of Western Washington: The Knowledge and Use of Indigenous Plants by Native Americans. University of Washington Press.

Harrington, C. (2024, May 2). Cedar advice [Personal communication].

Hartling, S., Sagan, V., & Maimaitijiang, M. (2021). Urban tree species classification using UAV-based multi-sensor data fusion and machine learning. GIScience & Remote Sensing. https://www.tandfonline.com/doi/abs/10.1080/15481603.2021.1974275

Heikkinen, V., Tokola, T., Parkkinen, J., Korpela, I., & Jaaskelainen, T. (2010). Simulated Multispectral Imagery for Tree Species Classification Using Support Vector Machines. IEEE Transactions on Geoscience and Remote Sensing, 48(3), 1355–1364. https://doi.org/10.1109/TGRS.2009.2032239

Hershey, K. T., Meslow, E. C., & Ramsey, F. L. (1998). Characteristics of Forests at Spotted Owl Nest Sites in the Pacific Northwest. The Journal of Wildlife Management, 62(4), 1398–1410. https://doi.org/10.2307/3802006

Hijmans, R. J. (2023). raster: Geographic Data Analysis and Modeling (3.6-26) [Computer software]. https://cran.r-project.org/web/packages/raster/index.html

Hijmans, R. J. (2024). terra: Spatial Data Analysis (1.7-71) [Computer software]. https://cran.r-project.org/web/packages/terra/index.html

Holmgren, J., Persson, Å., & Söderman, U. (2008). Species identification of individual trees by combining high resolution LiDAR data with multi-spectral images. International Journal of Remote Sensing, 29(5), 1537–1552. https://doi.org/10.1080/01431160701736471

Hologa, R., Scheffczyk, K., Dreiser, C., & Gärtner, S. (2021). Tree Species Classification in a Temperate Mixed Mountain Forest Landscape Using Random Forest and Multiple Datasets. Remote Sensing, 13(22), Article 22. https://doi.org/10.3390/rs13224657

Huang, J., & Ling, C. X. (2005). Using AUC and accuracy in evaluating learning algorithms. IEEE Transactions on Knowledge and Data Engineering, 17(3), 299–310. https://doi.org/10.1109/TKDE.2005.50

Hudak, A. T., Evans, J. S., & Stuart Smith, A. M. (2009). LiDAR Utility for Natural Resource Managers. Remote Sensing, 1(4), 934–951. https://doi.org/10.3390/rs1040934

Johnson, A., Clavijo, A. E., Hamar, G., Head, D.-A., Thoms, A., Price, W., Lapke, A., Crotteau, J., Cerveny, L. K., Wilmer, H., Petershoare, L., Cook, A., & Reid, S. (2021). Wood Products for Cultural Uses: Sustaining Native Resilience and Vital Lifeways in Southeast Alaska, USA. Forests, 12(1), Article 1. https://doi.org/10.3390/f12010090

Jones, K. (n.d.). Average Pond Values of Tree Species Over Time [Graph].

Kashani, A. G., Olsen, M. J., Parrish, C. E., & Wilson, N. (2015). A Review of LIDAR Radiometric Processing: From Ad Hoc Intensity Correction to Rigorous Radiometric Calibration. Sensors, 15(11), Article 11. https://doi.org/10.3390/s151128099

Kedzierski, M., Wierzbicki, D., Sekrecka, A., Fryskowska, A., Walczykowski, P., & Siewert, J. (2019). Influence of Lower Atmosphere on the Radiometric Quality of Unmanned Aerial Vehicle Imagery. Remote Sensing, 11(10), Article 10. https://doi.org/10.3390/rs11101214

Kline, N., Elder, V., & Fitzgerald, S. A. (2017). Managing Woodlands in the Coastal Fog Belt. Oregon State University Extension Service, EC 1131. https://extension.oregonstate.edu/sites/default/files/documents/ec1131.pdf

Koch, G. W., Sillett, S. C., Jennings, G. M., & Davis, S. D. (2004). The limits to tree height. Nature, 428(6985), 851–854. https://doi.org/10.1038/nature02417

Korpela, I., Ørka, H., Maltamo, M., Tokola, T., & Hyyppä, J. (2010). Tree species classification using airborne LiDAR – effects of stand and tree parameters, downsizing of training set, intensity normalization, and sensor type. Silva Fennica, 44(2). https://doi.org/10.14214/sf.156

Kruper, A., McGaughey, R. J., Crumrine, S., Bormann, B. T., Bennett, K., & Bobsin, C. R. (2022). Using Airborne LiDAR to Map Red Alder in the Sappho Long-Term Ecosystem Productivity Study. Remote Sensing, 14(7), Article 7. https://doi.org/10.3390/rs14071591

Kuhn, M., & Wickham, H. (2020). Tidymodels: A collection of packages for modeling and machine learning using tidyverse principles [Computer software]. https://www.tidymodels.org/

Larson, A. J. L. J., & Franklin, J. F. F. F. (2010). The tree mortality regime in temperate old-growth coniferous forests: The role of physical damage. Canadian Journal of Forest Research. https://doi.org/10.1139/X10-149

Liang, X., Hyyppä, J., & Matikainen, L. (2007). DECIDUOUS-CONIFEROUS TREE CLASSIFICATION USING DIFFERENCE BETWEEN FIRST AND LAST PULSE LASER SIGNATURES. IAPRS, XXXVI(Part 3/W52), 253–257.

Margolis, H. A., Nelson, R. F., Montesano, P. M., Beaudoin, A., Sun, G., Andersen, H.-E., & Wulder, M. A. (2015). Combining satellite lidar, airborne lidar, and ground plots to estimate the amount and distribution of aboveground biomass in the boreal forest of North America 1. Canadian Journal of Forest Research. 45(7): 838-855., 45(7), Article 7. https://doi.org/10.1139/cjfr-2015-0006

Mason, C. L., Calhoun, J., & Lippke, B. (2005). Options for Cedar Mill Waste Utilization and Disposal in Western Clallam and Jefferson Counties [Working Paper]. Rural Technology Institute, College of Forest Resources, University of Washington. http://www.ruraltech.org/pubs/working/cedar_mill/

McGaughey, R. J. (n.d.). Fusionwrapr Package [Computer software]. https://github.com/bmcgaughey1/fusionwrapr

McGaughey, R. J. (2023a, April 28). Process2022Data.R. [Source Code]. https://github.com/bmcgaughey1/DroneLidarCode/blob/main/Rcode/Process2022Data.R

McGaughey, R. J. (2023b). FUSION/LDV: Software for LIDAR Data Analysis and Visualization (4.51) [Computer software]. http://forsys.sefs.uw.edu/software/fusion/FUSION_manual.pdf

McGaughey, R. J. (2024a, February 5). CompositeImages.R. [Source Code]. https://github.com/bmcgaughey1/DroneLidar2023/blob/main/Rcode/CompositeImages.R

McGaughey, R. J. (2024b, March 4). ClipAdjTreeData.R. [Source Code]. https://github.com/bmcgaughey1/DroneLidarCode/blob/main/Rcode/ClipAdjTreeData.R

McGaughey, R. J., Ahmed, K., Andersen, H.-E., & Reutebuch, S. E. (2017). Effect of Occupation Time on the Horizontal Accuracy of a Mapping-Grade GNSS Receiver under Dense Forest Canopy. Photogrammetric Engineering & Remote Sensing, 83(12), 861–868. https://doi.org/10.14358/PERS.83.12.861

McGaughey, R. J., Kruper, A., Bobsin, C. R., & Bormann, B. T. (2024). Tree Species Classification Based on Upper Crown Morphology Captured by Uncrewed Aircraft System Lidar Data. Remote Sensing, 16(4), Article 4. https://doi.org/10.3390/rs16040603

Michałowska, M., & Rapiński, J. (2021). A Review of Tree Species Classification Based on Airborne LiDAR Data and Applied Classifiers. Remote Sensing, 13(3), Article 3. https://doi.org/10.3390/rs13030353

Minkova, T. V., Devine, W. D., & Martens, K. D. (2024). T3 Watershed Experiment in the Olympic Experimental State Forest: 2016-2023 Implementation Report. Washington State Department of Natural Resources, Forest Resources Division. https://live-onrc.pantheonsite.io/wp-content/uploads/2024/01/T3-Implementation-Report_final_20240122.pdf

Morris, P. I., & Stirling, R. (2012). Western red cedar extractives associated with durability in ground contact. Wood Science and Technology, 46(5), 991–1002. https://doi.org/10.1007/s00226-011-0459-2

Nesom, G. (2001). WESTERN RED-CEDAR [USDA NRCS Plant Guide]. USDA, NRCS, National Plant Data Center & the Biota of North America Program.

Oksanen, J., Simpson, G. L., Blanchet, F. G., Kindt, R., Legendre, P., Minchin, P. R., O'Hara, R. B., Solymos, P., Stevens, M. H. H., Szoecs, E., Wagner, H., Barbour, M., Bedward, M., Bolker, B., Borcard, D., Carvalho, G., Chirico, M., Caceres, M. D., Durand, S., … Weedon, J. (2022). vegan: Community Ecology Package (2.6-4) [Computer software]. https://cran.r-project.org/web/packages/vegan/index.html

Olympic National Forest—Planning. (n.d.). USDA Forest Service. Retrieved May 7, 2024, from https://www.fs.usda.gov/main/olympic/landmanagement/planning

Pavel, D. M., Miller, G. B., & Pavel, M. J. (1993). Too Long, Too Silent: The Threat to Cedar and the Sacred Ways of the Skokomish. American Indian Culture and Research Journal, 17(3), 53–80. https://doi.org/10.17953/aicr.17.3.u0w12280rwn27l63

Quan, Y., Li, M., Hao, Y., Liu, J., & Wang, B. (2023). Tree species classification in a typical natural secondary forest using UAV-borne LiDAR and hyperspectral data. GIScience & Remote Sensing, 60(1), 2171706. https://doi.org/10.1080/15481603.2023.2171706

Roussel, J.-R., Auty, D., Coops, N. C., Tompalski, P., Goodbody, T. R. H., Meador, A. S., Bourdon, J.-F., de Boissieu, F., & Achim, A. (2020). lidR: An R package for analysis of Airborne Laser Scanning (ALS) data. Remote Sensing of Environment, 251, 112061. https://doi.org/10.1016/j.rse.2020.112061

Roussel, J.-R., Auty, D., De Boissieu, F., Sanchez Meador, A., Jean-Francois, B., Demetrios, G., Adaszewski, S., Steinmeier, L., & St-Onge, B. (2024). lidR: Airborne LiDAR Data Manipulation and Visualization for Forestry Applications (4.1.1) [Computer software]. https://cran.r-project.org/web/packages/lidR/index.html

RStudio Team. (2023). RStudio: Integrated Development Environment for R (4.3.0) [R]. RStudio, PBC. http://www.rstudio.com/

Shebitz, D. J., Reichard, S. H., & Dunwiddie, P. W. (2009). Ecological and Cultural Significance of Burning Beargrass Habitat on the Olympic Peninsula, Washington. Ecological Restoration, 27(3), 306–319. https://doi.org/10.3368/er.27.3.306

Shoot, C., Andersen, H.-E., Moskal, L. M., Babcock, C., Cook, B. D., & Morton, D. C. (2021). Classifying Forest Type in the National Forest Inventory Context with Airborne Hyperspectral and Lidar Data. Remote Sensing, 13(10), Article 10. https://doi.org/10.3390/rs13101863

Silge, J. (2020, March 26). Tuning random forest hyperparameters with #TidyTuesday trees data. Julia Silge. https://juliasilge.com/blog/sf-trees-random-tuning/

Sosa-Herrera, J. A., Vallejo-Pérez, M. R., Álvarez-Jarquín, N., Cid-García, N. M., & López-Araujo, D. J. (2019). Geographic Object-Based Analysis of Airborne Multispectral Images for Health Assessment of Capsicum annuum L. Crops. Sensors, 19(21), Article 21. https://doi.org/10.3390/s19214817

Stroh, N., Baltzinger, C., & Martin, J.-L. (2008). Deer prevent western redcedar (Thuya plicata) regeneration in old-growth forests of Haida Gwaii: Is there a potential for recovery? Forest Ecology and Management, 255(12), 3973–3979. https://doi.org/10.1016/j.foreco.2008.03.039

Trick, R. J. (2012). Interdicting Timber Theft in a Safe Place: A Statutory Solution to the Traffic Stop Problem. Seattle Journal of Environmental Law, 2(1).

Turner, N. C., & Bell, M. A. M. (1971). The ethnobotany of the Coast Salish Indians of Vancouver Island. Economic Botany, 25(1), 63–99. https://doi.org/10.1007/BF02894564

Turner, N. J., & Turner, K. L. (2007). Traditional food systems, erosion and renewal in Northwestern North America. CSIR, 6(1), 57–68.

Van Pelt, J. (2007, December 10). Forks—Thumbnail History. History Link. https://www.historylink.org/file/8397

Van Pelt, R. (2007). Identifying Mature and Old Forests in Western Washington. Washington State Department of Natural Resources. https://www.dnr.wa.gov/publications/lm_hcp_west_oldgrowth_guide_full_lowres.pdf

Vaughn, N. R., Moskal, L. M., & Turnblom, E. C. (2012). Tree Species Detection Accuracies Using Discrete Point Lidar and Airborne Waveform Lidar. Remote Sensing, 4(2), Article 2. https://doi.org/10.3390/rs4020377

Vlachopoulos, O., Leblon, B., Wang, J., Haddadi, A., LaRocque, A., & Patterson, G. (2022). Evaluation of Crop Health Status With UAS Multispectral Imagery. IEEE Journal of Selected Topics in Applied Earth Observations and Remote Sensing, 15, 297–308. https://doi.org/10.1109/JSTARS.2021.3132228

Wang, B., Liu, J., Li, J., & Li, M. (2023). UAV LiDAR and Hyperspectral Data Synergy for Tree Species Classification in the Maoershan Forest Farm Region. Remote Sensing, 15(4), Article 4. https://doi.org/10.3390/rs15041000

Western Redcedar Dieback. (n.d.). WSU Puyallup Ornamental Plant Pathology. Retrieved October 4, 2023, from https://ppo.puyallup.wsu.edu/plant-health-concerns/redcedar/

Wong, T.-T. (2015). Performance evaluation of classification algorithms by k-fold and leave-one-out cross validation. Pattern Recognition, 48(9), 2839–2846. https://doi.org/10.1016/j.patcog.2015.03.009

Wright, M. N., & Ziegler, A. (2017). ranger: A Fast Implementation of Random Forests for High Dimensional Data in C++ and R. Journal of Statistical Software, 77, 1–17. https://doi.org/10.18637/jss.v077.i01

Xie, Q., Dash, J., Huang, W., Peng, D., Qin, Q., Mortimer, H., Casa, R., Pignatti, S., Laneve, G., Pascucci, S., Dong, Y., & Ye, H. (2018). Vegetation Indices Combining the Red and Red-Edge Spectral Information for Leaf Area Index Retrieval. IEEE Journal of Selected Topics in Applied Earth Observations and Remote Sensing, 11(5), 1482–1493. https://doi.org/10.1109/JSTARS.2018.2813281

Yin, D., & Wang, L. (2019). Individual mangrove tree measurement using UAV-based LiDAR data: Possibilities and challenges. Remote Sensing of Environment, 223, 34–49. https://doi.org/10.1016/j.rse.2018.12.034

Zahn, M. J., Palmer, M. I., & Turner, N. J. (2018). "Everything We Do, It's Cedar": First Nation and Ecologically-Based Forester Land Management Philosophies in Coastal British Columbia. Journal of Ethnobiology, 38(3), 314–332. https://doi.org/10.2993/0278-0771-38.2.314

Zhang, K., & Hu, B. (2012). Individual Urban Tree Species Classification Using Very High Spatial Resolution Airborne Multi-Spectral Imagery Using Longitudinal Profiles. Remote Sensing, 4(6), Article 6. https://doi.org/10.3390/rs4061741